Optimizing Renewable Energy Integration for Sustainable Fuel Production: A Techno-Economic Assessment of Dimethyl Ether Synthesis via a Hybrid Microgrid-Hydrogen System

Mohammed M. Alotaibi [1,2] and Abdulaziz A. Alturki [3,*]

1   Department of Chemical Engineering, Imperial College London, London SW7 2AZ, UK; mma522@ic.ac.uk
2   King Abdullah Petroleum Studies and Research Center (KAPSARC), Riyadh 11672, Saudi Arabia
3   Department of Chemical and Materials Engineering, Faculty of Engineering–Rabigh Branch,
     King Abdulaziz University, Jeddah 21589, Saudi Arabia
*   Correspondence: aaaaltrki@kau.edu.sa

Abstract: This study offers an in-depth analysis and optimization of a microgrid system powered by renewable sources, designed for the efficient production of hydrogen and dimethyl ether—key elements in the transition toward sustainable fuel alternatives. The system architecture incorporates solar photovoltaic modules, advanced battery storage solutions, and electrolytic hydrogen production units, with a targeted reduction in greenhouse gas emissions and the enhancement of overall energy efficiency. A rigorous economic analysis was conducted utilizing the HYSYS V12 software platform and encompassing capital and operational expenditures alongside profit projections to evaluate the system's economic viability. Furthermore, thermal optimization was achieved through heat integration strategies, employing a cascade analysis methodology and optimization via the General Algebraic Modeling System (GAMS), yielding an 83% decrease in annual utility expenditures. Comparative analysis revealed that the energy requirement of the optimized system was over 50% lower than that of traditional fossil fuel-based reforming processes. A comprehensive assessment of CO_2 emissions demonstrated a significant reduction, with the integration of thermal management solutions facilitating a 99.24% decrease in emissions. The outcomes of this study provide critical insights into the engineering of sustainable, low-carbon energy systems, emphasizing the role of renewable energy technologies in advancing fuel science.

Keywords: renewable energy-based microgrid; hydrogen production; dimethyl ether (DME) synthesis; heat integration; CO_2 emissions reduction

1. Introduction

Growing reliance on petroleum-based fuels for transportation raises concerns about oil depletion, climate change, and environmental impacts [1]. This has spurred global interest in developing alternative, sustainable fuels, such as DME [2]. DME, a colorless gas with high energy density, is considered a highly promising substitute for diesel fuel in engines of compression-ignition function engines due to its superior cetane number, low autoignition temperature, and remarkable compression characteristics [3]. Moreover, the market demand for DME is anticipated to expand, with its utilization of existing petroleum fuels projected to reach production levels of 9.5 million metric tons per annum [4].

DME can be synthesized through various routes, either directly or indirectly, using a wide range of feedstocks, including natural gas, coal, and biomass [5]. The growing demand for renewable methanol has further intensified the exploration of DME synthesis pathways. Notably, studies conducted by Matzen et al. and Leonzio et al. have demonstrated that the combustion of DME significantly mitigates greenhouse gas emissions and reduces fossil fuel consumption [6,7].

Ambitious goals have been established to achieve carbon neutrality in the marine and aviation transportation sectors by 2050. Khalili et al.'s projections suggest that by the midpoint of the century, approximately 9% of maritime transportation, 19% of passenger aviation, and none of the freight aviation sector will have transitioned to electrification [8,9]. The newly presented Net Zero Emissions by 2050 scenarios in the International Energy Agency (IEA)'s Outlook for World Energy reveal varying estimates for global hydrogen production by 2050: 19,361 TWh in the 2021 report and 11,667 TWh in the 2022 report. Likewise, the latest International Renewable Energy Agency (IRENA) study forecasts a hydrogen production of 17,500 TWh under the 1.5 °C setting and anticipates that e-hydrogen and e-fuels will make up 14% of the overall demand for final energy [10]. However, certain sub-sectors within the industrial domain present challenges for direct electrification or straightforward decarbonization. Examples of these hard-to-abate segments incorporate the chemical industry and extremely high operating temperature processes, such as cement manufacturing and steel production. To support a low-carbon energy system on a broader scale, the introduction of hydrogen technologies as a possible energy carrier has been proposed, with hydrogen most likely being generated from renewable energy [11].

Hydrogen, a versatile energy carrier, can be used as a chemical fuel for electrical energy generation or heat and power generation, making it an applicable clean energy carrier with possibilities for transportation and storage [12]. Although hydrogen is already utilized in fertilizer production, petroleum refining, and methanol production at rates of 55%, 25%, and 10%, respectively, its applications in transportation and utility markets are still growing [13]. Being a clean energy carrier, hydrogen presents a logical and appropriate alternative to fossil fuels. Converting surplus energy into a chemical energy carrier like hydrogen or methane allows for the balancing of spatial and temporal energy supply and demand. Innovative energy storage technologies like Power-to-Gas (PtG) facilities are essential for a sustainable energy system that relies heavily on renewable energy sources [14].

Power-to-X (PtX) technologies encompass a range of processes that involve converting surplus renewable electricity into various energy carriers, such as hydrogen, e-methanol, and e-ammonia, as demonstrated across the entire industrial landscape [9,15–18]. Electricity-based fuels and chemicals produced from renewable energy sources could potentially substitute fossil fuels in situations where using renewable electricity directly is not possible [9]. Hydrogen could potentially replace coal in steel production, while synthetic fuels may be able to replace kerosene, heavy oil, and diesel in aviation and maritime sectors. Dispatchable power plants, such as gas turbines, can use synthetic natural gas or hydrogen as substitutes for fossil fuels. Developing electrofuels is crucial for achieving a practically carbon-neutral decarbonization process in industry and developing a predominantly greenhouse gas-free energy system [9,19].

This study not only aims to design a DME production line using captured carbon dioxide (CO_2) and green hydrogen but also compares its efficiency and sustainability with existing DME production technologies. CO_2 capture and utilization technologies are crucial for decreasing CO_2 emissions and reaching carbon neutrality. Green hydrogen, generated by electrolyzing water with renewable electricity, provides a sustainable and low-carbon hydrogen supply for the DME synthesis process. The DME production process follows an indirect chemical conversion route involving two parallel reactions—an exothermic reaction that yields methanol, shown by Equation (1), and a reverse water–gas shift (RWGS) reaction, shown in Equation (2) [18]. For both reactions, a bifunctional $Cu/ZnO/Al_2O_3$ catalyst was chosen due to its superior catalytic performance and stability. The synthesized methanol then undergoes dehydration in a separate reactor over an γ-Al_2O_3 catalyst, resulting in DME as the final product [19,20]. A comprehensive process flowsheet for the DME production process is developed, incorporating key unit operations and equipment.

$$CO_{2(g)} + 3H_{2(g)} \leftrightarrow CH_3OH_{(g)} + H_2O \qquad \Delta H_{298k} = -49.50 \, \text{kJ/mol} \qquad (1)$$

$$CO_{2(g)} + H_{2(g)} \leftrightarrow CO_{(g)} + H_2O_{(g)} \qquad \Delta H_{298k} = 41.20 \, \text{kJ/mol} \qquad (2)$$
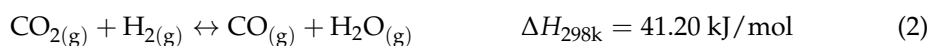
This is followed by a final reaction where the produced methanol is dehydrated in a separate reactor, as shown by Equation (3), over a γ-Al_2O_3 catalyst, giving rise to DME as the final product [21].

$$2CH_3OH_{(g)} \leftrightarrow CH_3OCH_{(g)} + H_2O_{(g)} \qquad \Delta H_{298k} = -23.50 \text{ kJ/mol} \qquad (3)$$

Recently, there has been a growing number of academic studies that have focused on examining the various production pathways associated with DME. For instance, Chen et al. (2016) evaluated the energy efficiency of different DME synthesis routes [20], while Falco et al. (2016) conducted a thermodynamic evaluation [21]. Luu et al. (2016) compared dry reforming and bi-reforming as preliminary steps for direct DME synthesis [22], and Matzen and Demirel (2016) performed a life cycle assessment, comparing DME production with renewable methanol [6]. Prasertsri et al. (2016) investigated syngas production via the dry reforming of methane [23], and Falco et al. (2017) examined the potential of a membrane reactor concept for direct synthesis of DME [21].

Other studies, such as Hankin (2017), investigated the thermodynamics of direct and indirect DME synthesis by comparing six syngas production routes [24]. Mevawala et al. (2019) performed a techno-economic evaluation of shale gas-to-DME production methods [25], while Michalios et al. (2019) assessed the techno-economics of DME synthesis from CO_2 within the Power-to-Liquids (PtL) concept [26]. Kartohardjono (2020) presented a case study that explored the utilization of CO_2 that is being captured from acid gas removal in existing gas processing plants for DME production [27]. This approach aimed to develop a sustainable method for repurposing CO_2 emissions into valuable fuel products. Rafiee (2020) explored approaches to optimize both direct and indirect DME synthesis pathways to enhance the efficiency and yield of the production process [28].

Bernardi et al. (2020) carried out a techno-economic investigation of direct DME synthesis, offering insights into the feasibility and performance of this particular route [29]. França Lopes et al. (2020) undertook a techno-economic assessment of DME production from an alternative biomass feedstock, sugarcane vinasse [30]. This study highlighted the potential of utilizing waste materials from the agricultural sector for DME production, contributing to a circular economy. Schemme et al. (2020) compared different synthetic energy carriers derived from hydrogen (H_2) and (CO_2) [31], including DME. Yasari et al. (2021) conducted a multi-objective optimization and techno-economic assessment for direct DME synthesis [32]. Wu and Chien (2022) focused on the analysis and optimization of process intensification options for producing DME from CO_2 [33]. Dieterich et al. (2023) investigated potential DME production routes by simulating various pathways and employing appropriate kinetic models [34]. These innovative methods, technologies, and strategies could streamline and intensify the process, further emphasizing the potential of CO_2 use in the sustainable production of alternative fuels.

Hybrid microgrid systems (HMGs) are increasingly vital for bringing electricity to rural areas. A variety of research (for example, [35–42]) has explored and suggested designs for hybrid renewable energy systems (HRES). These works offer comprehensive guidelines for creating standalone HRESs. The study cited as [35] delves into both the design and funding aspects of a microgrid located on the small island of Koh Jik. The HOMER (3.11 version) software was employed to examine the techno-economic landscape. In a similar vein, the research also weighed the influence of lead-acid versus lithium-ion batteries on both the levelized cost of energy (LCOE) and the share of renewables. The study referenced as [43] examines the best design for an (HRES)-integrated microgrid in a remote area of Saudi Arabia's Al Jouf region. The study investigates a microgrid configuration incorporating photovoltaic (PV) solar panels, wind turbines (WT), batteries, a diesel generator (DG), and an inverter using a social spider optimizer (SSO). The SSO identified the optimal configuration with a cost of energy (COE) of USD 0.13/kWh and a loss of power supply probability (LPSP) of 0.02. The study by Alturki (2022) aimed to provide an optimal design for a hybrid microgrid-hydrogen storage system in Saudi Arabia. It explored five distinct configurations for energy use in hydrogen generation. The study

indicates that the optimal setup for the specific site involves integrating solar, wind, battery, generator, fuel cell, and hydrogen electrolyzer elements. The ideal configuration has a net present value of USD 10.60 billion and a levelized energy cost of USD 0.15/kWh [44].

Zhenan et al. (2023) investigated the integration of PtX technology and Combined Heat and Power (CHP) into self-sufficient microgrids that use renewable energy sources. Case studies, including industrial sites and Karlsruhe harbor, demonstrate that such microgrids can be cost-competitive and environmentally friendly. The study emphasizes that the success of these systems is highly dependent on site-specific conditions and recommends the Power-to-Hydrogen and Hydrogen-CHP concept as the most promising technology variant. The research highlights the need for customized microgrid solutions to meet unique energy needs and achieve decarbonization [45].

Table 1 presents a comprehensive summary of simulation-based and techno-economic investigations into DME production [34]. The table delineates whether the study examined direct or indirect DME production, the primary carbon species investigated, and whether the research included in-depth kinetic modeling of DME formation reactions or solely relied on thermochemical equilibrium assumptions. Furthermore, the table indicates the presence of any economic evaluations.

Table 1. Summary of recent simulation-based and techno-economic investigations in the field of DME production.

Publication	Year	Direct	Indirect	CO	CO_2	Kinetic Modeling	Economic Evaluation	H_2 LCOH
Chen et al. [20]	2016	×	×	×	×			
Falco et al. [21]	2016	×			×			
Luu et al. [22]	2016	×		×		×		
Matzen and Demirel [6]	2016		×		×			
Prasertsri et al. [23]	2016	×	×	×	×			
Falco et al. [46]	2017	×	×	×	×	×		
Hankin [24]	2017	×	×	×	×			
Mevawala et al. [26]	2019	×	×	×			×	
Michalios et al.	2019		×		×	×	×	
Kartohardjono	2020	×	×		×	×		
Rafiee [28]	2020	×	×	×	×	×		
Bernardi et al. [29]	2020	×	×	×		×	×	
França Lopes et al. [30]	2020	×		×	×	×		
Schemme et al. [31]	2020		×		×		×	
Yasari et al. [32]	2021	×		×		×	×	
Wu and Chien [33]	2022							
Dieterich et al. [34]	2023	×	×	×	×	×	×	
This work			×		×	×	×	×

Many simulation studies have predominantly focused on energy and thermodynamic comparisons, relying on equilibrium modeling of the DME formation reaction. While these findings offer valuable insights into the energy efficiency, carbon conversion, and influence of process parameters, they may inadvertently overestimate conversion rates and complicate economic evaluations. This is primarily due to the limited consideration of reaction kinetics and the challenges of rigorously scaling reactors [47–50].

Nevertheless, many of these studies remain focused on specific routes, such as biomass-based production, direct CO_2 utilization, or an extensive comparison with alternative syn-

thetic energy carriers. As a result, drawing comparisons among potential DME production methods within the context of PtX becomes a complex task. This is because the intricacy of the simulations, the extent of heat integration considered, and the variation in economic boundary conditions substantially influence the final outcomes, making a straightforward comparison challenging in the field of chemical engineering.

This study aims to develop efficient and cost-effective CO_2 and hydrogen conversion methods into DME and integrate them with downstream chemical processes. Using the Aspen HYSYS V12 simulator, a techno-economic analysis was conducted to identify the most energy-efficient route for CO_2 and H_2 conversion into DME. Utilizing the GAMS optimizer to minimize external utility costs, we conducted interval-specific energy balance calculations for precision. Operating temperatures of the utilities and cost indexes are sourced from HYSYS, while the HOMER software is utilized to simulate a myriad of system configurations, selecting the most feasible solution based on the LCOE and green hydrogen requirements for the plant. In this study, we examine and contrast potential PtX alternatives for incorporating a techno-economic optimization that discloses the efficacy of each distinct hydrogen end-use option within a comprehensive smart energy system framework. This approach enables the diverse sectors to be interconnected synergistically.

2. Materials and Methods

2.1. Research Methodology

The process flowsheet is modeled using the Aspen HYSYS simulator, targeting an annual DME production capacity of 100,000 tons. Energy consumption, carbon footprint, total capital investment, and operating costs are employed to assess the proposed design's performance. Subsequently, heat integration is executed, aiming to maximize heat recovery within the system via a heat exchanger network (HEN). The primary objective is to identify the most economically viable and energy-efficient process for converting feedstocks into valuable chemicals while minimizing the environmental impact.

2.2. Model Initialization

The block flow diagram shown in Figure 1 is used to synthesize the simulation process. The selection of the Peng–Robinson Stryjek–Vera (PRSV) fluid package as the thermodynamic model in this study was a deliberate choice based on a thorough evaluation of available options. In comparison to the commonly used Soave–Redlich–Kwong (SRK) method, the PRSV method offers distinct advantages that align well with the specific demands of our DME synthesis process:
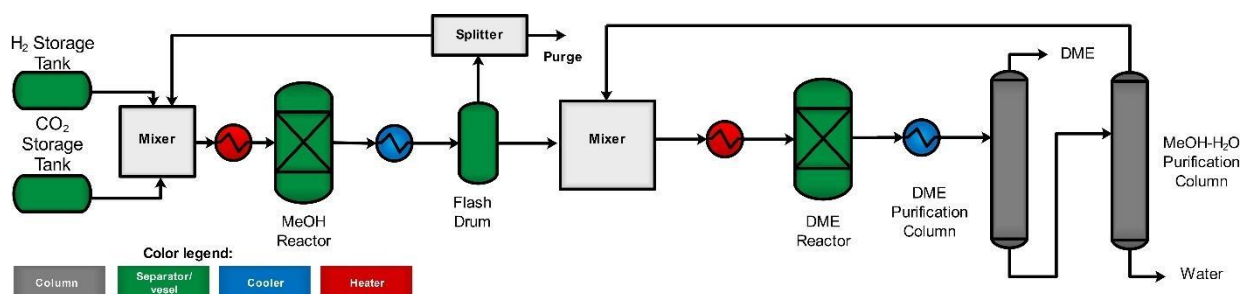

Figure 1. Block flow diagram for DME synthesis through CO_2 hydrogenations.

1. Accurate Handling of Aqueous Methanol Systems:

The PRSV package accurately predicts aqueous methanol systems, a key component of our method. While the SRK method can provide reasonable results for various systems, the PRSV method has shown better agreement with experimental data in scenarios involving methanol–water mixtures [51].

2. Accurate Prediction of Hydrogen Phase Behavior:

Hydrogen, being a key participant in the DME synthesis process, demands precise phase behavior predictions. The PRSV package has been well-established for its capability to accurately predict hydrogen behavior, offering an advantage over the SRK method in this context [51].

3. Optimum Package for Operating at Low Vapor Pressures:

Given that DME synthesis often occurs at low vapor pressures, the PRSV package stands out as particularly well-suited for such conditions. Its formulation excels in accurately capturing the complex interactions at play in systems with low vapor pressures, which is a relevant attribute for our study [52].

4. Previous Use in Similar Studies:

The widespread adoption of the PRSV package in studies closely related to DME synthesis attests to its reliability and suitability for this type of investigation. While both PRSV and SRK have their merits, the prevalence of PRSV usage in similar research, as documented in the literature [27,53], reinforces our confidence in its appropriateness for our study.

Hence, the selection of the PRSV fluid package over the commonly used SRK method stems from its demonstrated strengths in accurately handling aqueous systems containing methanol, accurately predicting hydrogen phase behavior, suitability for low vapor pressure conditions, and its established track record in similar studies. This decision ensures that our thermodynamic model aligns precisely with the nuances of our DME synthesis process, facilitating robust and accurate simulations.

The model kinetics used to simulate the process are described by Equations (4)–(6). The kinetic parameters and reaction rate expressions for the methanol synthesis, the RWGS side reaction, and the DME synthesis are presented in Table 2 [54,55]. A detailed kinetics calculation is available in Supplementary S1: Reaction constant calculations for a more comprehensive understanding of the kinetics calculations.

Table 2. Activation energy and pre-exponential factor for MeOH synthesis and dehydration reactions.

	MeOH Reaction Pre-Exponential Factor and Activation Energy			DME Reaction Pre-Exponential Factor and Activation Energy		
i	A_i	$E_{a,i}$	Ref	A_i	$E_{a,i}$	Ref
1	2.84×10^{-10}	-4.00×10^4		1.37×10^{10}	2.54×10^3	
2	3.45×10^3	0		1.24×10^{11}	2.51×10^4	
3	1.58×10^{-3}	-1.72×10^4		4.64×10^{-2}	-3.53×10^4	
4	6.63×10^{-16}	-1.24×10^5	[56]	8.47×10^{-2}	-4.22×10^4	[27]
5	3.25×10^5	9.81×10^4		-	-	
6	1.12×10^5	1.87×10^4		-	-	
7	3.04×10^3	5.84×10^4		-	-	

MeOH synthesis:

$$r_{CH_3OH} = \frac{k_1 P_{CO_2} P_{H_2} \left(1 - \frac{1}{K_{eq1}} \frac{P_{H_2O} P_{CH_3OH}}{P_{H_2}{}^3 P_{CO_2}}\right)}{\left(1 + k_2 \frac{P_{H_2O}}{P_{H_2}} + k_3 P_{H_2}{}^{0.5} + k_4 P_{H_2O}\right)^3} \left[\frac{kmol}{kg_{cat}s}\right] \tag{4}$$

$$r_{RWGS} = \frac{k_5 P_{CO_2} \left(1 - K_{eq2} \frac{P_{H_2O} P_{CO}}{P_{CO_2} P_{H_2}}\right)}{\left(1 + k_2 \frac{P_{H_2O}}{P_{H_2}} + k_3 P_{H_2}{}^{0.5} + k_4 P_{H_2O}\right)} \left[\frac{kmol}{kg_{cat}s}\right] \tag{5}$$

DME synthesis:

$$r_{DME} = \frac{k_1 C_{CH_3OH}^2 + k_2 C_{DME} C_{H_2O}}{\left(1 + k_3 C_{CH_3OH}^{0.5} + k_4 C_{H_2O}\right)^4} \left[\frac{mol}{m^3 h}\right] \tag{6}$$

Carbon Efficiency:

The carbon efficiency was determined by comparing the amount of carbon in the product to the amount of carbon in the feed stream according to Equation (7) [57].

$$\omega_C = \frac{\text{Carbon in DME product stream}}{\text{Carbon in inlet stream}} \tag{7}$$

2.3. HOMER Simulation

We used the HOMER software suite, known for its thorough examination of renewable energy systems, to conduct a detailed assessment including techno-economic evaluation and environmental impact analysis. We utilized an optimization technique to determine the most feasible system configuration [58]. The optimization process, including economic and environmental metrics, is visually summarized in Figure 2.
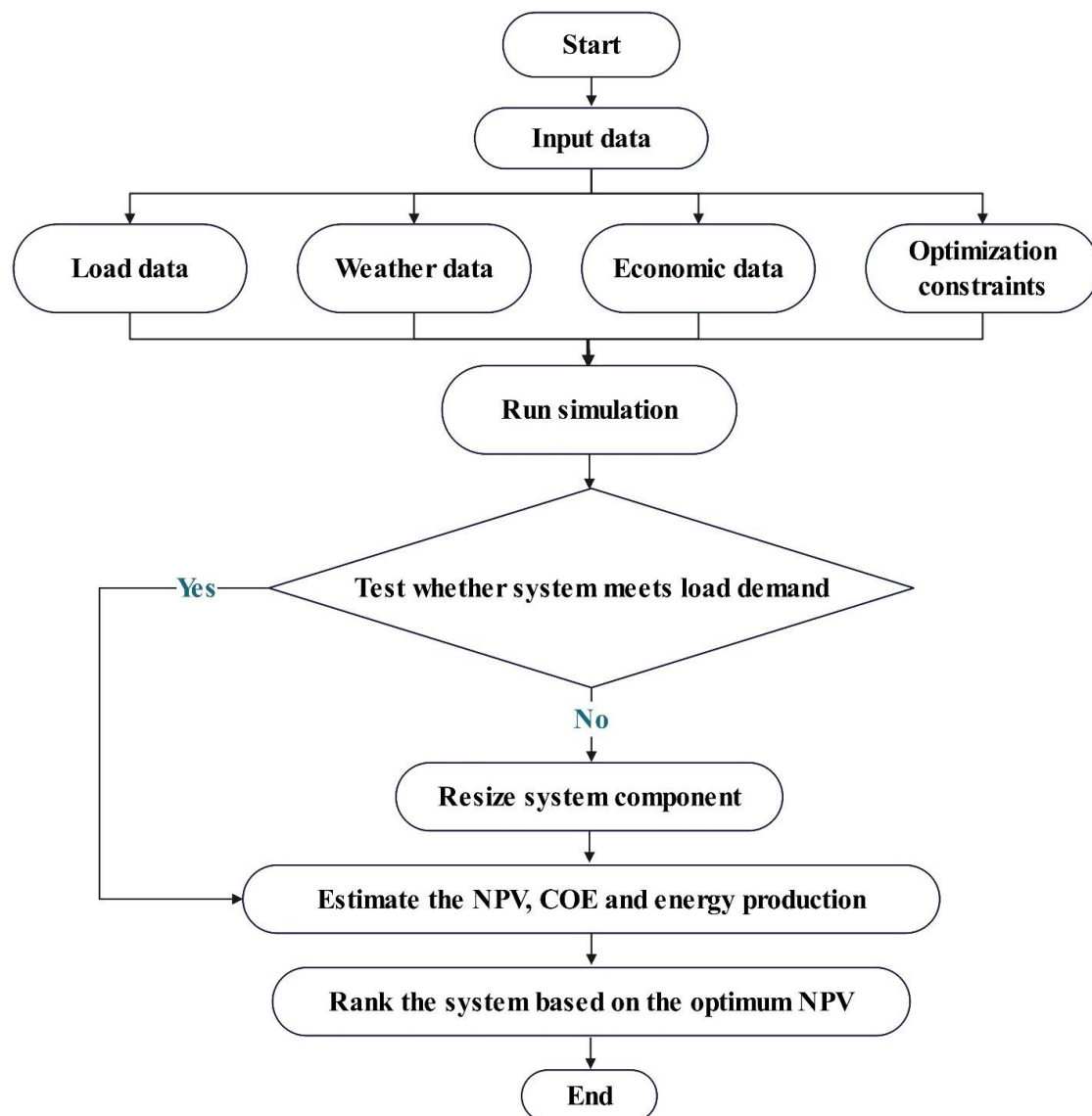

Figure 2. Optimization flowchart for HOMER.

The techno-economic assessment assumes that the costs of system components rise steadily. Calculations consider location-specific nominal interest rates (i) and yearly inflation rates (f). The projected project period is 25 years [59]. HOMER Pro computes the net present value (NPV) using the specified method:

$$NPV = \sum_{n=1}^{t} i_d \left(C_{Com} + C_{Rep} + C_{O\&M} + C_{Fuel} + C_{Sal} \right) \tag{8}$$

where i_d represents the discount rate, n is the project lifetime in years, C_{Com} stands for the capital cost of a system component, C_{Rep} is the replacement cost, $C_{O\&M}$ denotes the operation and maintenance (O&M) cost, C_{Fuel} signifies the fuel cost, and C_{Sal} represents the salvage value. Use this formula to calculate the discount rate i_d:

$$i_d = \frac{1}{(1+i)^n} \tag{9}$$

where i is the real annual interest rate, which can be calculated as follows using the nominal interest rate (i') and annual inflation (f) [60]:

$$i = \frac{i' - f}{1 + f} \tag{10}$$

In HOMER, the annualized cost is determined by initially calculating the project's *NPV* and subsequently multiplying it by the capital recovery factor (*CRF*), as demonstrated in the equation below:

$$C_{ann} = CRF(i, n) \times NPV \tag{11}$$

The *CRF* is a ratio employed to calculate the present value of an annuity (a sequence of consistent annual cash flows). The *CRF* formula is presented below:

$$CRF(i, n) = \frac{i(1+i)^n}{(1+i)^n - 1} \tag{12}$$

In HOMER, the *LCOE* is calculated as follows:

$$LCOE = \frac{C_{ann,tot} - c_{boiler} H_{served}}{E_{served}} \tag{13}$$

$C_{ann,tot}$ indicates the total yearly cost of the system; c_{boiler} represents the marginal cost of the boiler; H_{served} represents the total thermal load served; and E_{served} represents the total electrical load served.

In HOMER Pro, the following equation estimates the levelized cost of hydrogen (*LCOH*).

$$LCOH = \frac{C_{ann,tot} - v_{elec} \left(E_{prim,AC} - E_{prim,DC} - E_{def} + E_{grid,sales} \right)}{M_{H_2}} \tag{14}$$

$C_{ann,tot}$ is the total yearly cost, v_{elec} is the value of electricity, E_{prim} is the principal electrical load, E_{def} is the deferrable load, E_{grid}, sales is the amount of energy sold to the grid, and M_{H_2} is the total hydrogen generation.

2.4. Mathematical Modeling

The primary aim of this study is to identify an energy system configuration that minimizes GHG emissions and maximizes the renewable fraction (*RF*), with *RF* quantified by Equation (15) [61]. We evaluate three scenarios for each energy system—photovoltaic and wind—with and without the integration of battery and fuel cell storage, as illustrated in Figure 3 [61]. This comparative analysis seeks to determine the most cost-effective and reliable energy supply configuration for the Neom region.

$$RF = \frac{E_{ren} + T_{ren}}{E_{pro}} \tag{15}$$

E_{ren} is the energy produced from RE resources, while T_{ren} is the thermal energy produced from renewable resources. E_{pro} represents the overall energy production of the system, derived from renewable or nonrenewable sources.
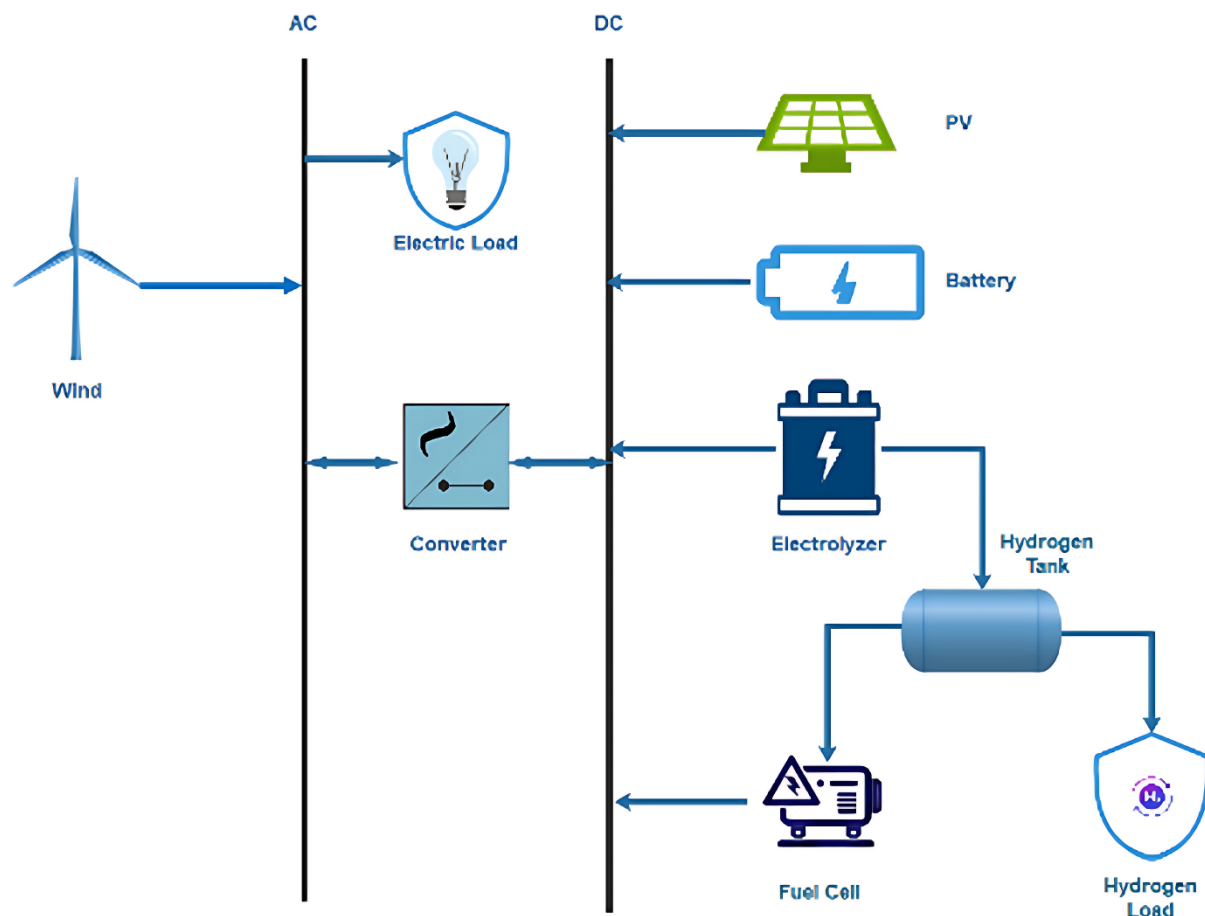

Figure 3. Schematic depicting system configurations for hydrogen production utilizing a battery bank and a fuel cell.

In scenarios where surplus energy is generated, an electrolyzer is employed to transform water into hydrogen. This hydrogen can be either sequestered for future use or immediately utilized to generate electricity via the fuel cell. This dual functionality, as simulated in HOMER, facilitates an enhanced energy storage strategy and promotes the efficient use of hydrogen as an energy vector.

Hydrogen storage is typically favored for long-term energy reserves owing to its substantial capacity, albeit with relatively modest energy-release rates compared to its storage potential. Conversely, the necessity for short-term electricity storage emerges to manage transient peaks in energy demand and to extend the operational life of fuel cells by ensuring a steady hydrogen supply. This short-term solution is characterized by a smaller storage capacity but benefits from a rapid energy release capability [44].

The comparative analysis of these scenarios is intended to yield a comprehensive and scientifically substantiated determination of the most advantageous energy system configuration. This configuration should be economically viable and environmentally sound, ensuring a dependable power supply. Our methodology provides an in-depth exploration of the dynamics between various energy storage methodologies and their influence on the overall efficacy and performance of the energy system.

2.5. Potential for Solar and Wind Energy in Neom, Saudi Arabia

In this study, our focus is on the Neom location, which is strategically located near the existing hydrogen plant under construction in Oxagon. The selection of this location is driven by the favorable combination of solar and wind resources, as well as its proximity to the emerging hydrogen hub in Neom and the planned development of 20 additional GW of renewable projects in the Neom area [62,63]. The choice of Oxagon as the proposed location for the plant is strategically aimed to supply DME while also creating synergy with a nearby project being developed by Neom Green Hydrogen Company. This adjacent project aims to generate 1.2 million metric tons of green ammonia annually. The co-location would facilitate integration and potentially optimize the supply chain for both initiatives [64].

To obtain the necessary weather data for our analysis, we access the NASA Atmospheric Science Data Center, which enables HOMER to extract location-specific data based on longitude and latitude coordinates. Figure 4 show the monthly averages of global solar radiation and wind speed for the selected area.
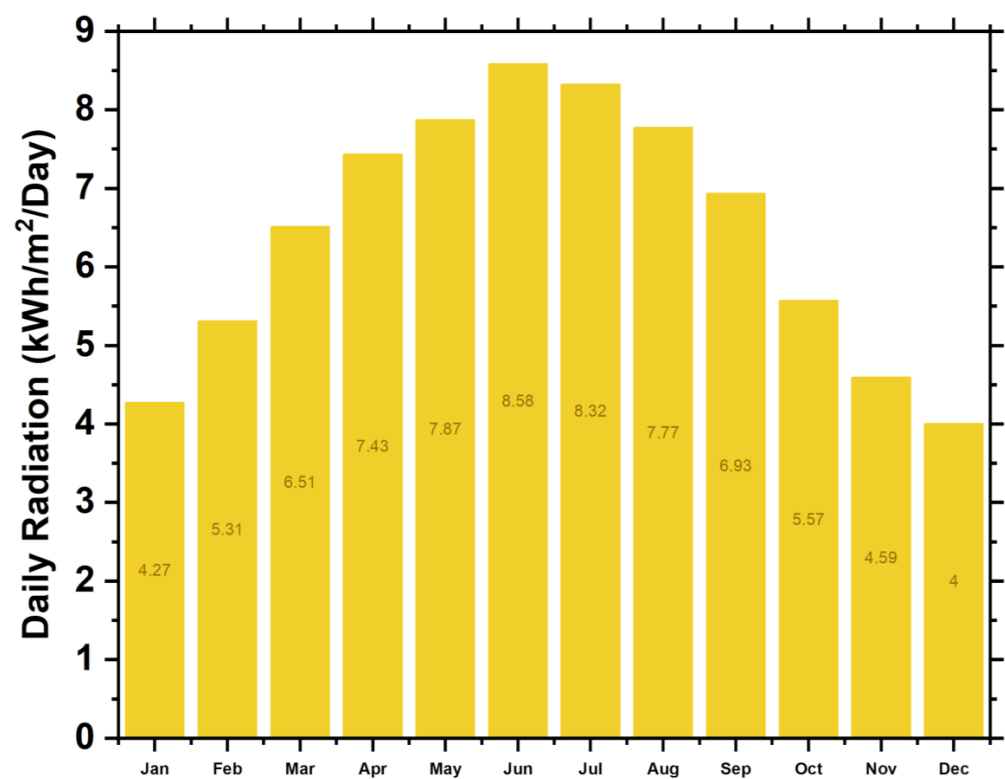

Figure 4. Seasonal solar potential.

Load demand greatly affects system reliability. We use unpredictability, daily changes, and hourly noise from two years of electric load profiles to generate load data. HOMER Pro collects 8760 hourly load data values from daily profiles at a site annually.

By conducting a comprehensive assessment of these factors, we aim to provide a cohesive and scientifically rigorous analysis of the optimal energy system configuration, considering the unique characteristics of the Neom location. This approach not only takes into account the available renewable resources but also addresses the challenges posed by variable load demand. Ultimately, it contributes to a more robust understanding of the overall system performance and the potential for further expansion in the region. The PV panel output can be expressed as follows [65]:

$$P_{pv} = I_S(t) \times \eta_{pv} \times A_{pv} \tag{16}$$

Solar irradiation I_S , PV panel area A_{pv}, and PV system efficiency η_{pv} are computed as follows:

$$\eta_{pv} = \eta_r \times \eta_t \times \left[1 - \beta \times (T_a \langle\, t\, \rangle - T_r) - \beta \times 1 < t > \times \left(\frac{NOCT - 20}{800} \right) \times (1 - \eta_r \times \eta_t) \right] \qquad (17)$$

NOCT represents the nominal temperature of operation of the cell in (°C). η_r represents baseline efficiency. η_t reflects the highest power point (MPPT) equipment efficiency. β is the temperature coefficient. T_a represents the ambient temperature in (°C), and T_r represents the cell reference temperature in (°C).

In NEOM, KSA, the PV potential is approximately 6.14 kWh/m^2/day. The highest solar irradiance is in June, while the lowest is in December. The system can generate the highest solar energy in June and the lowest in December. The solar potential of the site is presented in Figure 4.

Given the multitude of energy system component manufacturers available in the market, deriving an accurate representation of component costs is essential for a comprehensive analysis. To achieve this, we conducted a detailed review of the relevant literature and obtained data from various manufacturers. By aggregating and averaging the component costs, we generated a representative input for our study.

This approach ensures that our techno-economic assessment accounts for the diverse range of component costs in the market, leading to a more realistic and accurate evaluation of the optimal energy system configuration. Furthermore, by incorporating data from multiple sources, we mitigate potential biases and provide a more robust understanding of the financial implications associated with implementing different energy system configurations in a real-world context [66–73]. Table 3 displays the parameters of the solar system utilized in this investigation. A 100 kW solar system is a typical photovoltaic system that adds to the overall energy production of 1 GW. Figure 5 shows the energy demand for electricity annually.
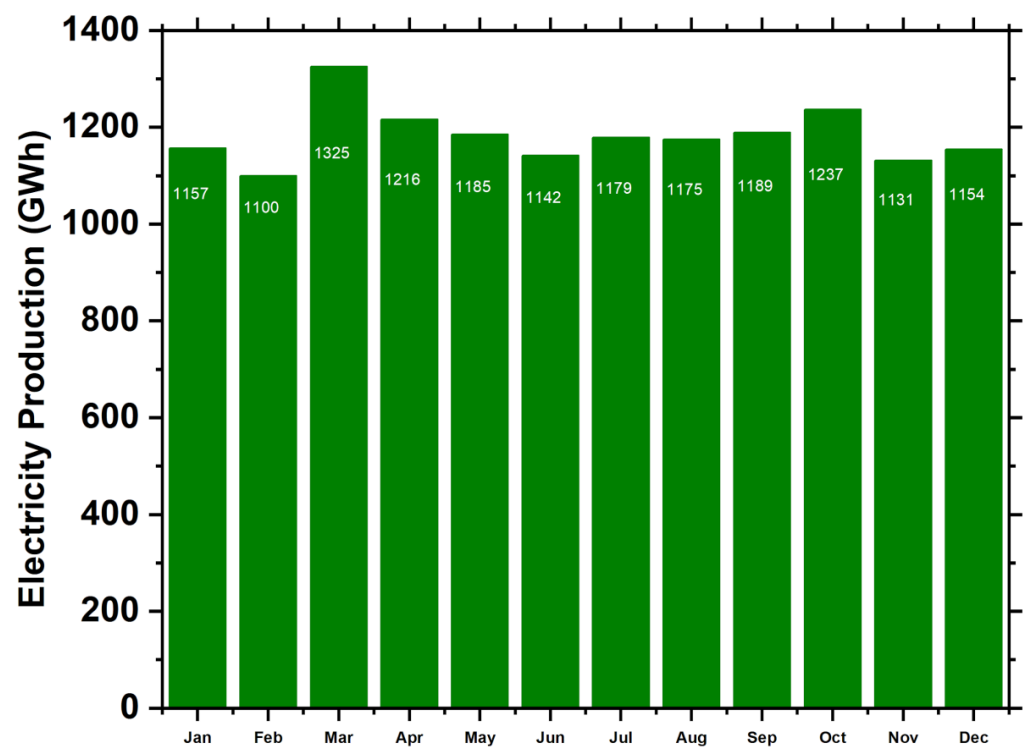

Figure 5. Energy demand.

Variable	Value
Initial Cost per Unit Value	USD 550/kWh
Cost of Replacing a PV system	USD 200/kWh
Lifetime	30 years

Wind power is directly proportional to wind speed and can be stated as [75]:

$$P_{wind} = \left\{ a \times V \times <t>^3 - b \times 0, \ V<t> \leq V_{Ci}, \ V<t> \geq V_{CO} \ P_r, V_{Ci} < V<t> < V_r \ P_r, V_r \leq V<t> < V_{CO} \right\} \quad (18)$$

Wind speed is denoted by V; wind-rated power is denoted by P_r; cut-in, cut-out, and rated wind speeds are denoted by V_{Ci}, V_{CO}, and V_r accordingly; a and b are two constants determined as follows:

$$\left\{ a = P_r / \left(V_r^3 - V_{Ci}^3 \right) \ b = V_{Ci} / \left(V_r^3 - V_{Ci}^3 \right) \right\} \quad (19)$$

The rated power of wind is calculated in the following manner:

$$P_r = \frac{1}{2} \times \rho \times A_{wind} \times C_p \times V_r^3 \quad (20)$$

where ρ indicates the air density, A_{wind} indicates the of a wind turbine, and C_p represents the wind resource at the Neom location that exhibits significant potential for power generation. With a yearly average wind speed of 4.72 m/s on a scaled basis, the site demonstrates a viable capacity for harnessing wind power. Seasonal variations in wind speed are observed, with the highest speeds occurring in July and the lowest in October. A visual representation of the wind potential can be found in Figure 6.
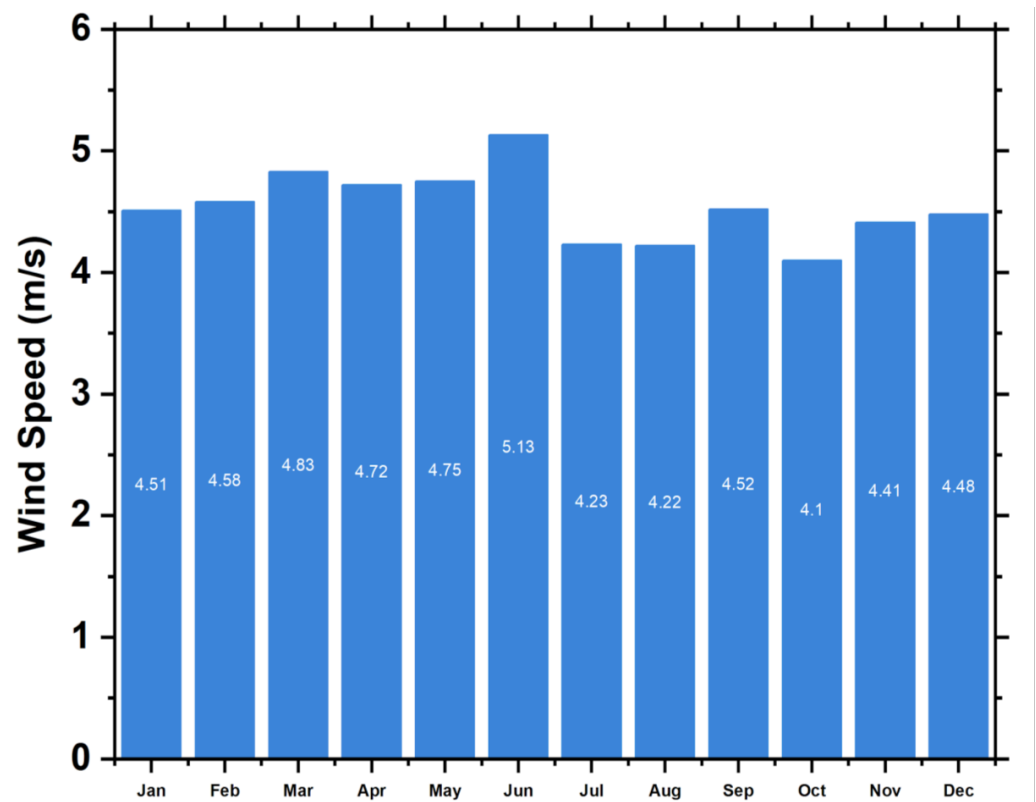
Figure 6. Seasonal wind speed (m/s).

To ensure a comprehensive analysis of the wind power potential at the Neom site, we carefully considered the specifications of the wind turbine to be employed in this study. These requirements, which include factors such as rotor diameter, hub height, and rated power, are detailed in Table 4. By taking into account the unique characteristics of the wind resource at Neom and the specifications of the selected wind turbine, our investigation aims to provide a cohesive and scientifically rigorous assessment of the potential for wind power production in this region.

Table 4. Specifications for wind turbine [66–73].

Variable	Value
Initial Cost per Unit Value	USD 520/kW
Cost of Replacing a Wind Turbine	USD 520/kW
Lifetime	20 years

The RE potential at the chosen location indicates that an HRES can be effectively implemented for power generation. While it is possible to meet the energy demand using conventional power plants, such as coal and fossil fuel-based plants, this approach would have a detrimental impact on the environmental health of the area due to the hazardous emissions produced by these facilities. Consequently, adopting an HRES strategy becomes essential in addressing the energy crisis while simultaneously preserving the environment and promoting a green, sustainable method of energy production.

Considering the aforementioned criteria, the site presents an ideal opportunity for the development of an HRES project. By harnessing the available renewable resources, the proposed system offers a viable alternative to traditional power generation methods, mitigating the environmental consequences associated with conventional power plants and contributing to a more sustainable energy landscape for the region.

2.6. Energy Storage via Battery/Hydrogen

Battery storage is an essential element in self-contained microgrid systems. The battery's capacity can be quantified in kilowatt-hours (kWh) [76]:

$$C_{bat} = \frac{E_l \times AD}{DOD \times \eta_{inv} \times \eta_b} \tag{21}$$

where η_{inv} and η_{inv} are inverter and battery efficiency (%), DOD the discharge penetration that prevents achieving the minimum state of the battery, and E_l is the total energy to be transferred; AD is autonomy of the battery.

The SOC is proportional to the battery current by

$$SOC(t) = SOC(0) + \frac{1}{C} \int_0^t I_B(V_{bat}, t') dt' \tag{22}$$

where denotes the battery's capacity, denotes the battery's current, and denotes the battery's voltage.

C, I_B , and V_{bat} represent the battery's capacity, current, and voltage, respectively.

A 4.20 MWh lithium-ion battery model with an initial investment cost of USD 175 per kWh is connected to our 250 kW system. The battery's initial state of charge is 100%, and the lowest charge state is 40%. Table 5 displays the economic factors and specifications of the battery.

The system utilizes 500 kW converters for the conversion process, which have a lifespan of around 15 years and operate at an efficiency of about 95%. The converter's properties are detailed in Table 6.

Table 5. Financial and performance considerations battery [66–73].

Variable	Value
Efficiency	90%
Initial Investment	50,000 USD
Maximum Limit	7.03×10^3 Ah
Cost of Replacing a Battery	50,000 USD
Annual Operation and Maintenance Cost	5000 USD
Voltage	600 V
Capacity	4 MWh

Table 6. Conditions for converter [66–74,77].

Variable	Value
Initial Cost per Unit Value	USD 300/kW
Cost of Replacing a Battery per Unit Value	USD 100/kW
Lifetime	15 years

Typically, the hydrogen flow generated by fuel cells is given by the following equation:

$$q_{H_2}^{req} = \frac{N_0 N_S I}{2FU} \tag{23}$$

where $q_{H_2}^{req}$ represents the necessary hydrogen flow to meet load. N_0 represents fuel cell stacks, N_S series cells per stack, and U represents utilization rate.

Hydrogen storage can be thought of as an ideal battery that can accept hydrogen (like "charging") and release it (like "discharging") as needed within its storage capacity, regardless of pressure, temperature, or dynamic factors.

Upon further examination, the quantity of stored hydrogen can be represented by the state of hydrogen (*SOH*2), a concept analogous to the state of charge (*SOC*) in batteries. This relationship can be mathematically expressed as follows (Equation (15)):

$$SOH2(t) = SOH2(0) + \frac{1}{C_H} \int_0^t \dot{m}_H(p, t') dt' \tag{24}$$

where $\dot{m}_H$ is the hydrogen mass flow rate, C_H is the gravimetric capacity of the storage, and p is the hydrogen pressure.

By characterizing hydrogen storage in this manner, we can gain a deeper understanding of its behavior and performance, ultimately enabling the development of more efficient and optimized energy storage systems that integrate hydrogen as a viable energy carrier. This, in turn, contributes to the advancement of clean and sustainable energy solutions in the context of an evolving energy landscape.

Figure 7 shows how we synthesized data by considering randomness with daily and hourly noise inputs after scaling the annual daily average to 800 tons of daily production. With a 25-year lifespan, a hydrogen tank costs 300 USD/kW of hydrogen to build and repair (Table 7) [66,67,78].

Table 7. Cost data for hydrogen systems [66,67,78,79].

Components	Variable	Value
Fuel Cell (FC)	Initial Investment Cost per Unit Value	USD 3000/kW
	Cost of Replacing a Fuel Cell	USD 3000/kW
	Lifetime	40,000 h
Electrolyzer	Initial Investment Cost per Unit Value	USD 300/kW
	Cost of Replacing an Electrolyzer per Unit	USD 300/kW
	Lifetime	20 Years
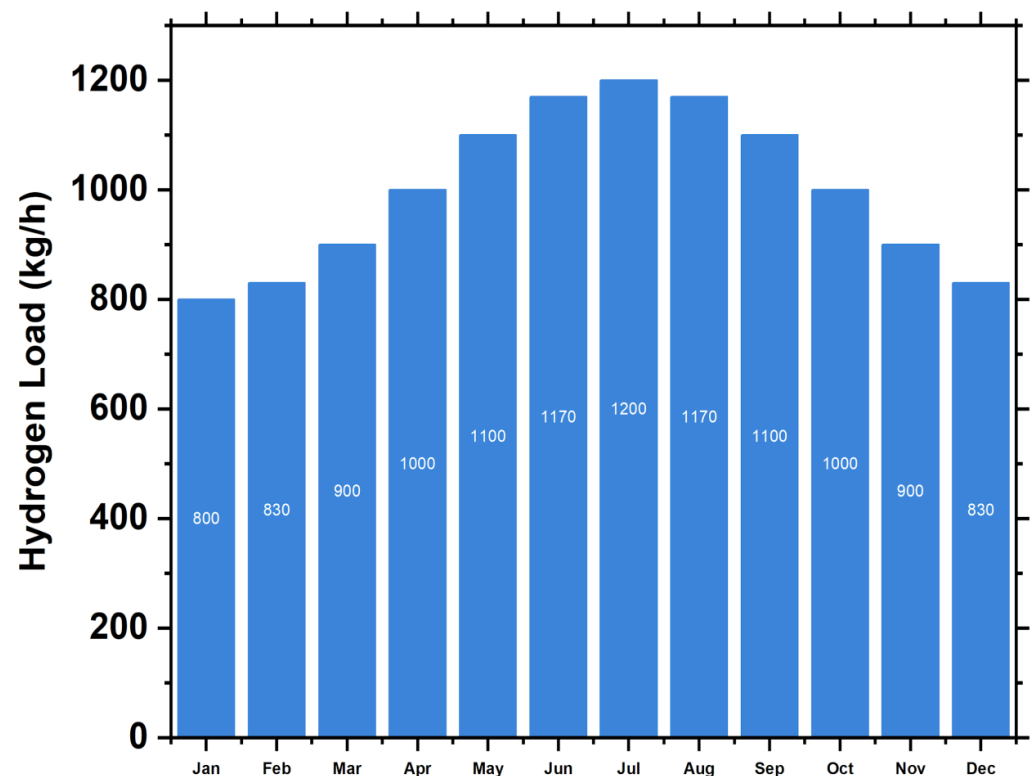
Figure 7. Hydrogen load demand annually.

2.7. Heat Exchanger Network Development

The methodological framework of this study encompasses the systematic development of an HEN with an emphasis on minimizing external heating and cooling requirements. HEN was created to calculate the least external heating and cooling utility needs. The enthalpy changes between heat exchangers were derived from the HYSYS simulation and utilized to calculate the heat capacity mass flow rate (CP) for each stream. The minimal temperature difference was set at Δ_{Tmin} = 20 K.

The pinch analysis HEN diagram, a crucial component of the HEN methodology, was constructed based on the identified pinch temperatures: the cold pinch temperature of 372 K and the hot pinch temperature of 392 K. Three main criteria were taken into consideration when stream matching. Firstly, above the pinch, the cold stream heat capacity must be greater than or equal to the hot stream heat capacity, and vice versa. Secondly, above the pinch, the total number of cold streams must be greater than or equal to the hot streams, and vice versa. Thirdly, the minimum temperature difference between the hot and cold streams, known as the minimum approach temperature, must be carefully determined. In this study, we assumed a minimum approach temperature of 20 K.

This choice is pivotal as the minimum temperature difference serves as a cornerstone for the subsequent design and optimization of the heat exchange network. It significantly impacts the heat exchanger sizing, utility requirements, and overall energy efficiency. A smaller temperature difference reduces the demand for additional utilities, yet it necessitates progressively larger heat transfer surfaces, thereby leading to larger heat exchangers [80]. The decision to use a 20 K minimum approach temperature is subject to a trade-off between operational and capital expenses. While a lower approach temperature improves energy utilization, it might lead to increased capital costs due to the larger exchanger sizes. Conversely, a higher approach temperature might reduce capital expenses but could result in less efficient energy usage. Therefore, selecting the appropriate minimum approach temperature involves careful consideration of both operational and capital factors.

The minimum number of heat exchangers can be calculated as a function of the number of streams (N_S) and the total number of external hot and cold utilities (N_U) used, as shown by equation Equation (22) [81].

$$N_{HX,min} = N_S + N_U - 1 \tag{25}$$

3. Process Description

The proposed design follows an indirect method, whereby the process can be divided into two distinctive phases: methanol synthesis by CO_2 hydrogenation and DME production by methanol dehydration. This method was chosen as it is currently the most commercially viable process, with many studies published on the kinetics of DME synthesis over solid–acid catalysts. A block flow diagram (BFD) of the developed process is shown in Figure 1.

The design approach was formulated according to the raw material parameters specified in Table 8, utilizing green hydrogen generated by water electrolysis and CO_2 obtained from direct air capture.

Table 8. Feed stream compositions.

Component	H$_2$ Feed Stream	CO$_2$ Feed Stream	Ref
H$_2$	99.90 mol %	-	[82]
H$_2$O	0.10 mol %	-	
CO$_2$	-	98 mol %	[83]
N$_2$	-	2 mol %	

In a recent article, Stepanenko and Kneba 2019 identified the optimum ratio for methanol synthesis of H_2/CO_2 to be 3:1 [5]. Therefore, an H_2/CO_2 feed stream ratio of 3:1 was used to encourage the production of methanol. The feed stream pressures of 30 bar and 20 bar were used for H_2 and CO_2, respectively. The temperature of the feed streams was assumed to be at a storage tank temperature of 273 K. Both feed streams were compressed to 79.5 bar and mixed with a recycle stream. The mixed stream was then heated by a heat exchanger to 483 K and fed into a methanol synthesis reactor. In a study by Kumar (2006), it was concluded that the pressure drop across a heat exchanger varies from 0.10 to 2.30 bar [84]. The pressure drop in the heat exchanger was anticipated to be 1.50 bar. The reactor operates at a constant temperature of 483 K and a pressure of 78 bar [85]. According to some studies, the commercial $Cu/ZnO/Al_2O_3$ catalyst was shown to be a suitable catalyst for producing methanol from CO_2 hydrogenation [50,56,86,87]. A catalyst mass of 44,500 kg was adapted from similar research [56]. The specifications of this catalyst for methanol synthesis are provided in Table 2. As shown in Equations (1) and (2), both the synthesis of methanol and RWGS reactions occur simultaneously in the methanol reactor. The product stream leaving the methanol reactor was depressurized and cooled down to be flashed at 65 bar and 303 K to separate the products from the unreacted gasses [88]. The gasses that were not fully reacted and exited the flash drum through the top

stream were either returned to the reactor to improve the conversion rate or released into the atmosphere to prevent by-product buildup. A renewable methanol synthesis research project recommends a recycle stream purge ratio of 0.10, and therefore, this ratio has been adapted to the design process [85]. The product stream leaving the flash unit was further depressurized and heated to 17.50 bar and 573 K, including a pressure drop of 1.50 bar across the heat exchanger.

The stream was sent into a DME reactor operating at 17.50 pressure and 573 K for methanol dehydration. Research articles indicate that the reaction can take place on several solid–acid catalysts, such as γ-alumina and modified-alumina with silica and phosphorus, at temperatures ranging from 523 to 673 K and pressures of up to 18 bar [89–91]. Methanol dehydration using modified-alumina catalysts with silica reduces coking and by-products [92]. Hence, the DME synthesis reaction is carried out over γ-Al_2O_3 and is shown in Equation (3) [50]. Yaripour et al. concluded that at the aforementioned operation conditions, the following parameters were achieved: a methanol conversion rate (X_{MeOH}) of 78.17%, a DME selectivity rate (S_{DME}) of 99.98%, and a yield rate (Y_{DME}) of 78.19% [93]. The catalyst mass was assumed to be 44,500 kg, and the catalyst specifications for DME synthesis are available in Table 9.

Table 9. Commercial catalyst specifications.

	Cu/ZnO/Al$_2$O$_3$		γ-Al$_2$O$_3$	
Parameter	**Value**	**Ref**	**Value**	**Ref**
Density	1775 (kg$_{cat}$/m^3$_{cat}$)		2010 kg$_{cat}$/m^3$_{cat}$	
Fixed bed porosity	0.40	[54]	0.20	[94]
Conversion rate	33%		78%	

Following DME synthesis, the product stream undergoes depressurization to 10 bar and cooling to 393 K, a critical step for optimal functioning of the subsequent purification unit. The purification unit consists of two parallel distillation columns. DME was separated from the unreacted methanol, and water by-products were separated in the first distillation column and then gathered as the desired product. The column consists of 32 stages and is run at 10 bar and 393 K, with a reflux ratio of 1.87, leading to a DME product purity of 99.99 wt% or 99.99 mol% [95]. The liquid stream containing methanol and water from the first distillation column is fed into the second column, where unreacted methanol is separated and recycled, and the water by-product is sent to a water treatment unit. The column has 42 stages and is operated at an atmospheric pressure of 393 K, with a reflux ratio of 2.04, resulting in methanol product purity of 99.99 wt% or 99.99 mol% [95].

3.1. Flowsheet Design

The DME synthesis route involves a combination of two ongoing processes: renewable methanol synthesis and methanol dehydration. The process was designed based on heuristics, with literature sources used to aid in the design decisions and mass balance calculations carried out to support the design feasibility. The developed process flowsheet is given in Figure 8, and hereafter, in this section, all streams and equipment refer to this figure.

The process flowsheet presents a streamlined chemical process for producing DME. Initially, feed streams (H_2 and CO_2) are pressurized via compressors (K-101, K-102, K-103), then combined in mixers (MIX-101). The mixed streams undergo temperature regulation in heat exchangers (E-101) before entering the methanol reactor (R-101; post-reaction, the streams are cooled (E-102) and then separated in a flash drum (V-101). MIX-102 combines process streams with recycled methanol before they are introduced to Heat Exchanger E-103. The stream then enters the DME Reactor R-102, where H_2 and CO_2 are catalytically converted into DME.
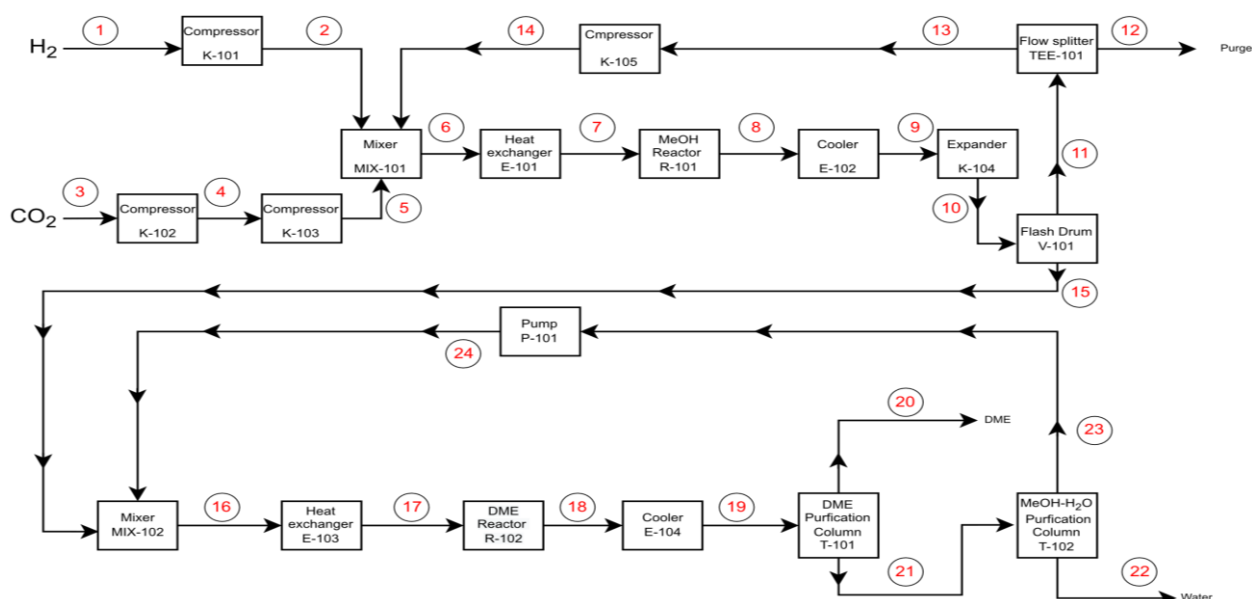
Figure 8. Developed process flow diagram.

Post-reaction, the mixture is directed to Cooler E-104, essential for subsequent separation stages. The product stream is then fed into the DME purification column T-101, where DME is separated from impurities and by-products to meet product specifications. Parallel to this, any methanol–water mixture produced is processed through the methanol–H_2O purification column T-102 to separate and purify methanol for recycling.

3.1.1. Batch vs. Continuous Process

In the context of bulk chemical production, particularly for an annual target of 100,000 tons of DME, it is essential to consider the most effective type of process—batch or continuous. Contrary to smaller-scale productions, bulk chemical manufacturing necessitates a focus on both efficiency and scalability.

According to a study by Leuenberger et al., continuous processes offer advantages for high-volume processes, particularly in the realm of bulk chemicals where large quantities are produced [96]. They allow for more efficient use of both time and resources, resulting in a more streamlined operation that can meet the target production levels.

Goršek and Glavič's work complements this viewpoint by highlighting the drawbacks of batch processes in such high-capacity scenarios [97]. Batch processes necessitate more expensive equipment with large capacities and are encumbered by higher filling, emptying, and heating/cooling times. Additionally, these processes require intermediate storage, further escalating costs and complexity.

For these reasons, and aligned with the specific needs of bulk chemical production, continuous processes are generally favored for operations targeting high annual outputs, such as the 100,000 tons/year scale considered for DME production in this study.

3.1.2. Input–Output Structure
Feed Stream Purification

In the context of our proposed system, which targets an annual production of 100,000 tons of DME, feed stream purity is paramount. The feed streams (S1 and S2) have been designed to meet stringent quality criteria consistent with industry standards, thus eliminating the need for a separate purification step under specified conditions [98]. The previous literature on similar high-scale chemical processes has shown that a feed purification unit was neither employed nor recommended due to high-efficiency downstream separation mechanisms already in place [47,56,99].

Recycle and Purge

In light of chemical engineering fundamentals, it is understood that achieving complete conversion in reactors is often limited by chemical equilibrium constraints. Due to these thermodynamic limitations, a portion of unreacted materials is expected to exit the reactors. To mitigate this, we incorporated recycling processes (referenced as S13 and S23) to increase the efficiency of the overall system by reusing unreacted reactants [100].

Considering the system operates under isochoric conditions and the feed streams are not purified, the presence of inert gasses like nitrogen (N_2) could contribute to an increase in total system pressure. We recognize that this increased pressure, coupled with unreacted materials, could present a safety hazard [101]. Therefore, a purge system is implemented, whereby 10% of the recycle stream (S10) is purged to prevent the accumulation of inert gasses and unreacted materials, thereby ensuring the system operates safely within its design constraints [102].

Number of Product Streams

Three streams leave the overall process. The stream of purge gasses (S12) is released into the atmosphere, the condensed water stream (S22) exits to the water treatment unit, and the desired DME stream (S20) is collected as a final product.

3.1.3. Equipment Selection

Reactors

The selected process employs continuous operation, eliminating the need for batch reactors. Given the gaseous state of the reactants in the methanol synthesis (R-101) and dehydration (R-102) reactions, solid catalytic reactors, specifically packed bed reactors, are used instead of continuous stirred-tank reactors [81]. Packed bed reactors offer a higher solid surface area, leading to enhanced conversion per unit weight of catalyst [103].

Both methanol synthesis and dehydration processes are exothermic and highly favored at lower temperatures. Therefore, operating temperatures are carefully controlled: 483 K for methanol synthesis and 573 K for dehydration. Temperature control is performed by using heating coils to shift the equilibrium toward the generation of products in a thermodynamically beneficial manner [50,92].

In the methanol synthesis reaction, the equilibrium is also affected by the concentration of the limiting reactant, CO_2. To maximize product formation, the H_2/CO_2 feed ratio is maintained at 3, enhancing the CO_2 concentration [93]. Additionally, the pressure is another parameter affecting equilibrium; it is optimized to maximize methanol formation. For methanol synthesis, the operating pressure is set to the maximum allowable pressure of 78 bar [104]. In contrast, the operating pressure for the DME reaction is set to the minimum allowable pressure of 17.50 bar, as the number of moles of reactants and products is equal, rendering the reaction's equilibrium position insensitive to pressure changes [85]. Detailed parameters for both reactors are provided in Table 10 [93].

Table 10. Methanol synthesis and dehydration reactor specifications.

	MeOH Synthesis Reactor (R-101)		MeOH Dehydration Reactor (R-102)	
Parameter	**Value**	**Ref**	**Value**	**Ref**
Operating temperature	483 (K)		573 (K)	[93]
Operating pressure	78 (bar)		17.50 (bar)	
Reactor length	5 (m)	[85]	8 (m)	
Reactor diameter	1 (m)		4 (m)	[94]
Number of tubes	1000 (tubes)		1	
Catalyst	$Cu/ZnO/Al_2O_3$		$\gamma\text{-}Al_2O_3$	
Conversion rate	$X_{CO2} = 33\%$	[54]	$X_{CH3OCH3} = 78.17\%,$	[93]
Yield	$Y_{CH3OH} = 99\%$		$Y_{CH3OCH3} = 78.19\%$	
Selectivity	$S_{CH3OH} = 99\%$		$S_{CH3OCH3} = 99.98\%$	

Pressurizing and Depressurizing

At the methanol synthesis phase, the desired feed streams (S1 and S3) have pressures of 79.5 bar, accounting for a pressure drop of 1.50 bar across the heat exchanger. However, streams S1 and S3 have pressures of 30 bar and 20 bar, respectively. Based on heuristics, a compressor is required to attain a pressure greater than 2.06 bar, although when the outlet/inlet pressure ratio is greater than 3, a staged compressor system is required [81]. Hence, a single compressor (K-101) is used to pressurize S1 from 30 bar to 79.50 bar with a pressure ratio of 2.65. However, S3 required a two-stage gas compressor system (K-102 and K-103) as the gas compression ratio is greater than 3. According to heuristics, the compressor ratio should be similar to a multi-stage gas compression system [81]. Therefore, S3 was pressurized from 20 bar to 79.50 bar through a two-stage compressor system (K-102 and K-103), where the compression ratio was held at 1.99 throughout. The methanol product (S9) was depressurized by an expander where its pressure decreased from 75.90 bar to 65 bar. The recycled methanol stream (S23) was in a liquid phase, where its pressure increased from 1 bar to 16.50 bar by a pump (P-101).

Heating and Cooling

The mixed feed stream (S5) was heated from 420 to 573 K to meet the operating temperature of R-101 via a shell and tube heat exchanger (E-101), which operates in a counter-current mode due to its high efficiency [105]. The methanol product (S6) is cooled down via a counter-current flow shale tube heat exchanger (E-102) from 483 K to 303 K. The mixed methanol stream (S15) is also heated from 303 K to 573 K via a counter-current flow shale tube heat exchanger (E-103).

One- and Two-Phase Separations

Due to lowering the pressure and the temperature of the methanol product stream (S7), partial condensation was achieved. Furthermore, the low temperature and pressure stream (S9) was fed into a flash drum which operates at 303 K and 65 bar, where a liquid–vapor phase separation takes place [88]. Due to the operating temperature (303 K) of the flash drum, pure methanol and water were collected in the bottom stream as their boiling temperatures were 337.80 K and 373 K, respectively [106]. Due to poor conversion, S17 at R-102 was a ternary mixture of DME, water, and methanol. Two parallel distillation columns separated the mixture. The first column yields pure DME, and the second column recycles methanol [95]. The specifications of the purification columns are shown below in Table 11.

Table 11. DME and methanol–water purification column specifications.

	DME Distillation Column (T-101)		MeOH-H_2O Distillation Column (T-102)	
Parameter	**Value**	**Ref**	**Value**	**Ref**
Operating T	393 (K)		393 (K)	
Operating P	10 (bar)		1 (bar)	
Column diameter	1.30 (m)		1.70 (m)	
Number of stages	32	[95]	42	[95]
Feed stage	16		23	
Reflux ratio	1.87		2.04	
Product purity	DME = 99.99 (mol%)		MeOH = 99.99 (mol%)	

3.2. Process Adjustment

In this chapter, all streams and equipment are in reference to Figure 1 unless stated otherwise. In the methanol synthesis phase of the design, the ratio of CO_2 to H_2 in the stream before entering reactor R-101 was adjusted to 1:7 to maximize the conversion of methanol synthesis [85]. To achieve this, the expander (K-104) was removed, and a valve (V-101) was placed before the cooler (E-102) to decrease the pressure of the produced

methanol until it reached the same operating pressure as the flash drum. The purpose of this modification was to ensure that the pressure of the methanol stream was compatible with the flash drum. It should be noted that in the heuristics-based flowsheet design (Figure 1), the expander (K-104) was utilized but could only operate when the stream was in the vapor phase to avoid abrasion.

The methanol synthesis reaction produces a significant amount of water, which can impede the methanol dehydration process [107]. To address this issue, an additional distillation column (T-101) was strategically placed between the flash drum (V-101) and the second reactor (R-102) to remove the excess water formed in the first reactor. This separation of water helps drive the methanol dehydration reaction forward, resulting in an increased conversion rate, in accordance with Le Chatelier's principle.

To ensure the effective removal of CO_2 residues, a partial condenser was employed. In cases where the temperature of the condenser might not be sufficiently low, the partial condenser facilitates the release of CO_2 from the system. The stream from the condenser within T-101, which contains CO_2 and other components, serves as part of the feedstock and is mixed with the recycled methanol from T-103.

Furthermore, a valve (VLV-102) was added upstream to regulate the pressure and achieve the desired atmospheric pressure in the system. This valve helps control the pressure conditions within the distillation column. The parameters of the simulated distillation column (T-101) can be found in Table 12.

Table 12. Simulated distillation column parameters.

	T-101	**T-102**	**T-103**
Parameters	**Value**	**Value**	**Value**
Operating Temperature	304 (K)	473 (K)	380 (K)
Operating Pressure	1 (bar)	13.17 (bar)	1.50 (bar)
Condenser Pressure	1 (bar)	12 (bar)	1.50 (bar)
Reboiler Pressure	1 (bar)	12 (bar)	1.50 (bar)
Total number of stages	21	4	20
Feed stage	11	3	7
Reflux ratio	1.08	1.33	5.53
Product purity	MeOH = 99 (mol%)	DME = 90 (mol%)	MeOH = 84 (mol%)

To achieve the desired operating pressure of 16.5 bar in PFR-102, P-101 was added after MIX 102. This addition helped maintain the required pressure level for the efficient operation of PFR-102. In T-102, a full reflux condenser was utilized to produce DME in the vapor phase. This choice was made to address the presence of impurities, such as CO_2, in the DME product. By employing a full reflux condenser, the condenser temperature could be controlled to prevent it from dropping too low, thus ensuring efficient separation of impurities. The purity of the DME product in T-102 was set to 90%, which is the highest purity attainable based on the simulation data from the shortcut column. Details regarding this purity and related parameters can be found in Table 12.

Consideration was given to the operating costs associated with cooling utilities. If the outlet temperature of the condenser in T-102 is too low, it will lead to increased consumption of cooling utilities, thereby raising costs. Hence, the decision to maintain a lower purity of 90% in T-102 was made to ensure a profitable and economically feasible process.

To facilitate the transportation and storage of DME, E-105 was incorporated to cool the DME products to the liquid phase at 298 K. This step allows for easier handling and storage of DME. Furthermore, the valve VLV-103 was added to decrease the operating pressure to 1.50 bar in T-103, situated between the T-102 reboiler and T-103. By reducing the pressure, the total reflux condenser could be used to produce liquid methanol at 1.50 bar. This liquid

methanol serves as the driving force for the stream to recycle back and mix with the stream from T-101.

3.3. Simulated Process

The DME production process was simulated, as shown in Figure 9. The simulated process features a mix of equipment, including mixers, heat exchangers, reactors, coolers, a flash drum, and a purification column, along with associated piping and instrumentation details. Each piece of equipment is tagged with identifiers (e.g., MIX-102, E-103, R-102), and the diagram includes process streams with specified temperature, pressure, and flow conditions, delineated by color-coded lines that represent different phases or types of streams—such as feed, product, or recycle streams.
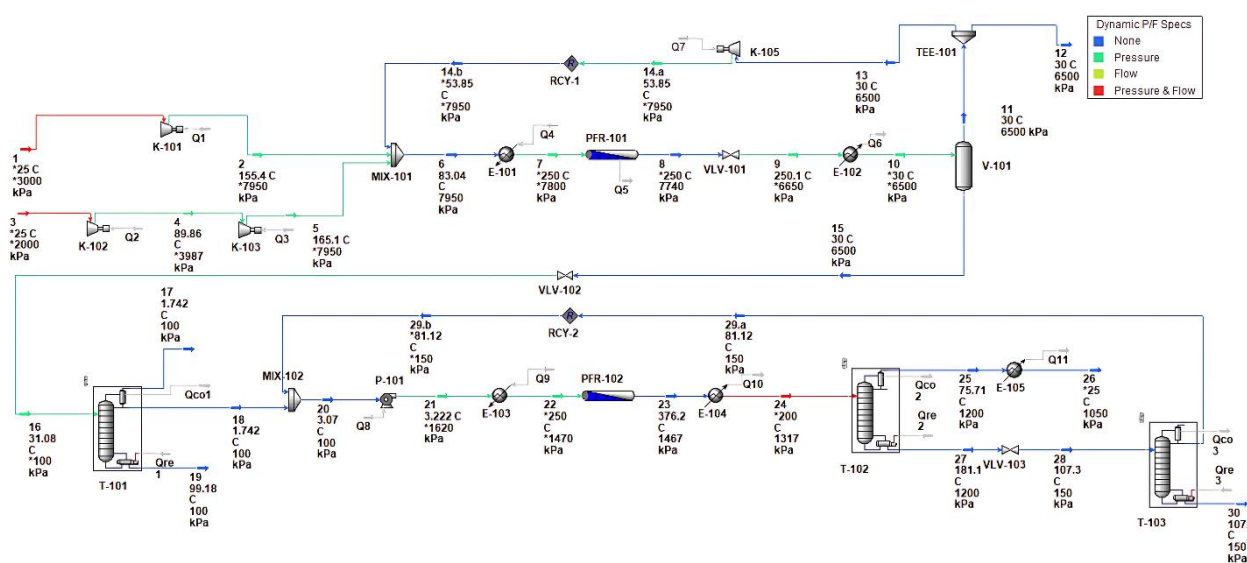

Figure 9. Simulated process.

After Mixer MIX-101, the process stream is conditioned in E-101 and then undergoes a reaction in methanol reactor R-101. Post-reaction, the stream is cooled in E-102 and subsequently enters V-101 for separation; methanol is channeled toward MIX-102 and then to E-103 for further temperature adjustment. This conditioned stream feeds into the second reactor, DME reactor R-102, where DME synthesis occurs. Following this reaction, the stream is once again cooled in E-104 before being purified in the DME purification Columns T-101 and T-103.

4. Results

This study aims to analyze the cost structure for such systems, taking into consideration the LCOE, NPV, and O&M costs.

Our analysis revealed that the estimated LCOE for PV plants integrated with battery systems is 4.90 cents/kWh, which is consistent with the average LCOE for solar energy in 2022 [79]. The total NPV for the system is found to be USD 3.30 billion, with the battery storage systems accounting for 30% of the cost, PV modules contributing 61%, and the power conversion systems and other balance of system components constituting the remaining 9%. Additionally, the annual O&M costs for the system are estimated to be USD 29 million. For this system, the solar capacity is 4 GW, and the levelized cost of the solar system alone, without accounting for other components, is 1.90 cents/kWh. The capacity factor is 21%, and the nominal battery capacity is 22 GWh. The storage wear cost is USD 0.01/kWh, and the total annual electricity production is 8.20 GWh/year.

In the second case analysis, we examine the integration of wind turbines with battery storage systems to compare the LCOE with that of PV plants. In this scenario, the estimated

LCOE using wind turbines combined with battery systems is 12.80 cents/kWh. The total NPV for the system amounts to USD 8.70 billion, with battery storage systems accounting for 41% of the cost, wind turbines contributing 54%, and power conversion systems and other balance of system components constituting the remaining 5%. The O&M costs are estimated to be USD 26 million. For this system, the wind capacity is 7 GW, and the levelized cost of the wind system alone, without accounting for other components, is 3.10 cents/kWh. The capacity factor is 19%, and the nominal battery capacity is 87 GWh. The storage wear cost remains at USD 0.01/kWh, and the total annual electricity production is 11 GWh/year. This analysis illustrates that, although wind turbines integrated with battery storage systems have a higher LCOE compared to solar PV, they offer a greater electricity production capacity.

In the third case analysis, we consider adding a hydrogen electrolyzer to the first case of PV with batteries to compare the LCOE. In this scenario, the estimated cost of electricity using only PV plants associated with battery systems is 6.30 cents/kWh. The NPV for the system is USD 4.40 billion, with PV modules contributing 74% and the remaining 26% being attributed to the battery, electrolyzer, power conversion systems, and other balance of system components. The annual O&M costs are estimated to be USD 42 million. For this system, the PV capacity is 7.50 GW, and the levelized cost of the solar system alone, without accounting for other components, is 1.90 cents/kWh. The capacity factor is 21.50%, the nominal battery capacity is 12.40 GWh, and the storage wear cost is USD 0.01/kWh. The total annual electricity production is 14.20 GWh/year. Figure 10 illustrates the economic analysis of three case studies: (1) PV systems integrated with energy storage systems (ESS), (2) wind turbine systems integrated with ESS, and (3) PV systems enhanced with ESS and an electrolyzer for hydrogen production.
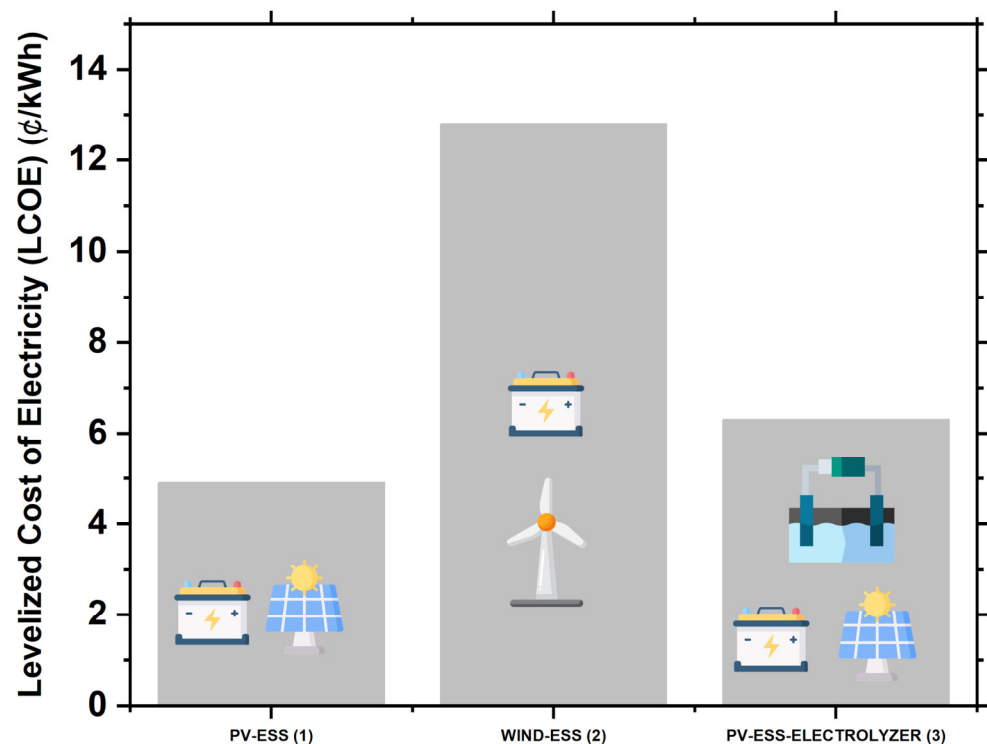

Figure 10. Comparative analysis of integrated renewable energy systems.

For the PV and battery system, the LCOE stands at 4.90 cents per kWh, with an NPV of USD 3.30 billion and annual O&M costs estimated at USD 29 million. When wind turbines are integrated with battery storage, the LCOE rises to 12.80 cents per kWh, the total NPV increases to USD 8.70 billion, and the annual O&M is around USD 26 million. Adding a hydrogen electrolyzer to the solar PV and battery setup results in an LCOE of 6.30 cents

per kWh and increases the total NPV to USD 4.40 billion, with annual O&M costs rising to USD 42 million.

The total capital expenditure (CapEx) was evaluated using HYSYS economic analysis and found to be USD 1.91×10^7/yr. The catalyst costs were determined based on their respective masses, with the cheapest selling prices of $Cu/ZnO/Al_2O_3$ and $\gamma\text{-}Al_2O_3$ being USD 43.50/kg and USD 14/kg, respectively. Similarly, the operating expenses were determined to be USD 7.32×10^7/yr, including the raw material and catalyst costs.

The LCOH estimated for this system using the HOMER software is found to be USD 12.80/kg of H_2, taking into consideration the capital cost of the entire system. Another approach to calculating LCOH is to use the LCOE and electrolyzer capital cost as inputs for the LCOH calculation. Given the LCOE of 6.30 cents per kWh (USD 0.06/kWh) and an electrolyzer capital cost of USD 300/kW, we can estimate the LCOH based on the approach outlined in the previous answer. We will keep the same assumptions for electrolyzer efficiency (70%), electrolyzer lifetime (25 years), fixed O&M cost (2% of capital cost per year), and hydrogen production rate (44 kg per MWh). Using these assumptions and the revised LCOE, the LCOH is USD 3.54 per kg of hydrogen.

The economic analysis incorporates a captured CO_2 selling price at USD 0.01/kg. For an accurate feasibility assessment, we based our profit calculations on a DME selling price set at USD 1092.96 per ton. The total annual profit, based on the achieved DME production capacity, was estimated to be USD 1.37×10^7/yr. However, it is important to note that this profit evaluation is a rough estimate, as a discount factor was assumed to be negligible. Table 10 summarizes the main economic parameters. The total CapEx was determined using HYSYS economic analysis and found to be USD 1.91×10^7/yr. Additionally, catalyst costs were assessed based on the respective masses of $Cu/ZnO/Al_2O_3$ and $\gamma\text{-}Al_2O_3$, with the lowest selling prices at USD 43.50/kg and USD 14/kg, respectively [26,108]. Operating expenses, including the cost of raw materials and catalysts, amounted to USD 7.32×10^7/yr.

In the comprehensive analysis of the proposed microgrid system, a key aspect to consider is the total energy consumption. Utilizing the HYSYS energy analyzer, the annual energy consumption was calculated to be 2.06×10^{12} kJ/yr (Table 13). This evaluation is crucial for understanding the energy efficiency of the system and its potential impact on the environment.

Table 13. Energy consumption analysis via HYSYS.

Energy Category	Unit	Quantity
Electricity	kWh/year	4.23×10^7
Hot utilities	kJ/yr	1.17×10^{12}
Cold utilities	kJ/yr	1.85×10^{12}

Furthermore, the total utility costs associated with the microgrid system were determined to be USD 8,979,510/yr. A detailed breakdown of these costs, including the contributions from various utilities used in the system, can be found in Table 14. This information provides a comprehensive insight into the economic viability of the suggested design and its suitability for real-world applications.

When evaluating the proposed system's performance, it is crucial to consider carbon efficiency as a vital parameter. Carbon efficiency is the ratio of carbon in the DME product stream to the carbon in the inlet stream, represented as a percentage in Equation (7).

This analysis reveals that the proposed design process exhibits a carbon efficiency of 86%. This finding highlights the effective utilization of carbon resources within the system, contributing to its overall sustainability and environmental performance. The high carbon efficiency demonstrates the system's potential to minimize greenhouse gas emissions and support a low-carbon energy future.

Table 14. Economic parameters analysis.

Category	Unit	Quantity
CapEx	USD	19,060,400
OpEx	USD/yr	73,199,650
Revenue	USD/yr	105,989,621
Profit	USD/yr	13,729,571

The economic analysis is based on 8000 operation hours~one year.

The methanol synthesis reaction achieved a conversion rate of 44.77%, while the RWGS side reaction exhibited a conversion rate of 0.32%. Additionally, the methanol dehydration reaction demonstrated a conversion rate of 89.81%. The carbon efficiency was within the estimated value, and the annual profit was valued at USD 8,231,378.

4.1. HEN Pinch Temperature Identification

To accurately carry out heat integration, Table 15 was created to summarize the required parameters for the target streams. After maximizing the heat recovery within the system, the total external heating and cooling utilities required were found to be 5.12×10^7 kJ/h and 1.04×10^8 kJ/h, respectively. A detailed calculation of the pinch analysis is available in Supplementary S3—HEN Diagram Construction.

Table 15. Streams summary table used for heat integration.

Number	Equipment	State	CP (kJ/°C·h)	T_S (K)	T_S adjusted (K)	T_t (K)	T_t adjusted (K)	ΔH (kJ/h)
1	E-101	Cold	298,042.17	356.04	366.04	523	533	49,760,000
2	E-102	Hot	502,881.47	523.13	513.13	303	293	110,700,000
3	T-101 Condenser	Hot	246,864.69	409.30	399.30	348.70	338.70	14,960,000
4	T-101 Reboiler	Cold	1,046,842.11	452.20	462.20	454.10	464.10	1,989,000
5	E-103	Cold	133,885.26	276.22	286.22	523	533	33,040,000
6	E-104	Hot	38,120.15	649.18	639.18	473	463	6,716,000
7	T-102 Condenser	Hot	331,558.44	361.80	351.80	354.10	344.10	2,553,000
8	T-102 Reboiler	Cold	559,300	380.30	390.30	381.30	391.30	559,300
9	E-105	Hot	123,891.15	348.71	338.71	298	288	6,282,000
10	T-103 Condenser	Hot	876,479.51	340.60	330.60	274.70	264.7	57,760,000
11	T-103 Reboiler	Cold	60,370,000	372	382	373	383	60,370,000

4.2. HEN Diagram

The HEN diagram reflecting this approach is presented in Figure 11. For a comprehensive breakdown of stream matching, refer to Supplementary S3: HEN Diagram Construction. The figure displays an energy flow diagram with input streams S1 to S11, indicated in blue, feeding into a series of process units denoted by white circles. Red lines represent the flow of energy within the system, with the flow direction is marked by arrows. Energy values at each stage are provided in kilowatts (kW).

4.3. HEN Utilities Cost Optimization

Based on the HYSYS analysis, the total utility costs were USD 8,979,510/yr. GAMS optimizer was used to minimize the total cost of external utilities. Energy balance calculations were carried out at each interval, where the operating temperatures of the utilities and the cost indexes were acquired from HYSYS. The cost function and a detailed GAMS model builder are available in Supplementary S1: Utilities Cost Optimization. Different heating/cooling utilities were inserted, and based on the objective function, GAMS reported the optimum combination. The optimized utility costs were USD 1,499,828 annually (8000 h).

The total annual utility costs decreased by 83% from USD 8,979,510 to USD 1,499,828 via GAMS optimizer.
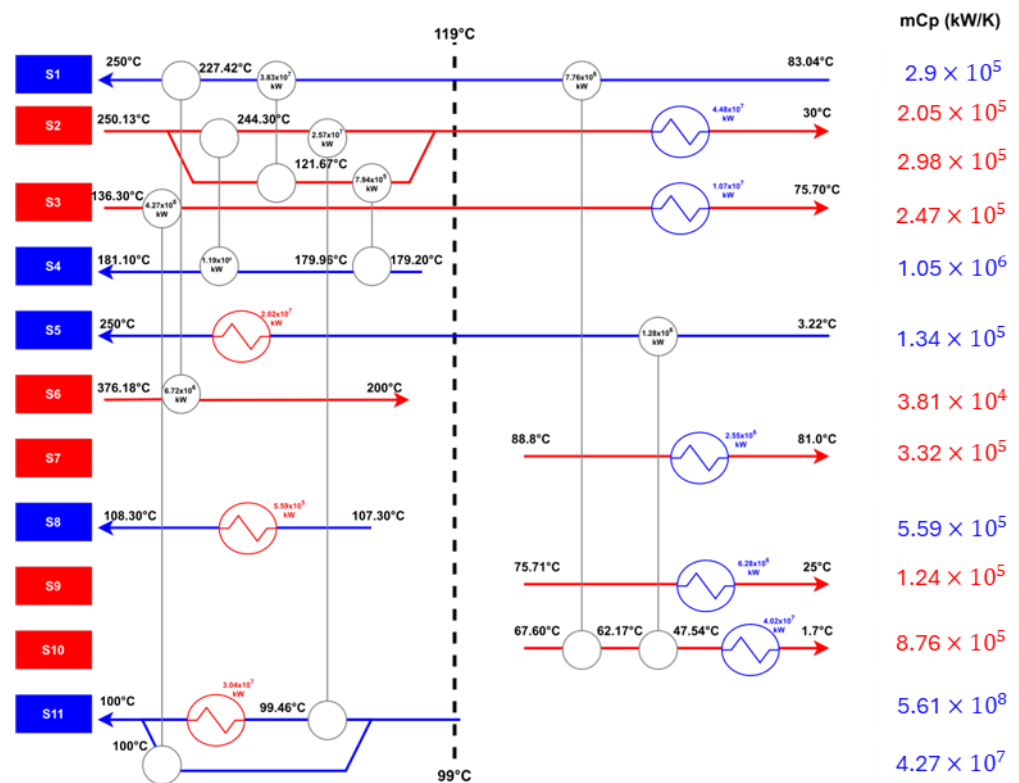

Figure 11. HEN for the proposed design process.

4.4. HEN Utilities Sources and Pinches

Based on the GAMS report (available in Supplementary S1: Figure D9), the optimum heating utilities are hot oil (HO) and low-pressure (LP) steam, representing 93% and 7% of total heating utilities, respectively. Other heat sources, such as fired heat (1000) along with high- and medium-pressure streams, were neglected by GAMS due to their high costs. Hence, HO was used for heating to achieve the maximum temperature of 649 K. The LP stream was also used since it is less expensive than other utilities. The total optimum cooling utilities are cooling water (CW) and a refrigerant (RG), accounting for 77% and 23% of total cooling utilities, respectively. The system was mainly cooled down using CW except for T-101 (in Figure 3), where RF was required to lower the stream temperature to 275 K. Additionally, as shown in the GAMS report available in Supplementary S1: Figure C10, the system displayed multiple pinch points, namely a process pinch (line 10) as well as high and low-temperature utility pinches (lines 2 and 17), each with a net heat flow of zero. The addition of external utilities is the cause of the utility pinch [109,110]. Using Equation (22), a total of 16 heat exchangers are needed, with 9 above the pinch and 7 below it. The minimum number of heat exchangers can be calculated as a function of the NS and the NU used, as shown by equation Equation (22).

5. Discussion

Integrating renewable energy with storage solutions, including batteries and hydrogen electrolyzers, marks a significant step toward a sustainable, low-carbon energy system. The analysis within this study, which evaluates the economic viability and environmental impact of PV systems, wind turbines, and hybrid systems incorporating hydrogen electrolysis, underscores several key insights and pathways for future research and development.

To compare these systems, it is essential to consider the trade-offs. Although the wind-based system has a significantly higher LCOE and total NPV, it offers a greater annual

electricity production of 11 GWh/year, compared to 8.20 GWh/year for the solar-based system. However, incorporating a hydrogen electrolyzer into the solar setup offers the benefits of long-term hydrogen energy storage, albeit at a slightly higher LCOE.

The calculation of LCOH using HOMER software yields an estimated USD 12.80/kg of H_2, factoring in the capital cost of the entire system. This figure is pivotal for understanding the economic feasibility of hydrogen production in the evaluated microgrid system. An alternative methodology for determining LCOH incorporates the LCOE and the capital cost of the electrolyzer as primary inputs. This alternative approach yields a revised LCOH of USD 3.54 per kg of hydrogen, significantly lower than the initial estimate provided by the HOMER software. This discrepancy highlights the sensitivity of LCOH calculations to the assumptions and methodologies employed. The initial estimate reflects a comprehensive consideration of the system's capital costs, while the alternative calculation focuses more narrowly on the costs directly associated with electricity and electrolysis. The substantial difference in LCOH between these two calculations underscores the importance of clearly defining the scope and parameters of LCOH estimations.

The alternative calculation equivalent to USD 3.54/kg is consistent with prices previously obtained from the literature ranging from USD 2.93 to USD 3.22/kg [108].

The ideal setups can produce a maximum of 26,291 tons of hydrogen annually. Using 26,291 tons of hydrogen per year for power generation instead of traditional natural gas power plants provides substantial environmental advantages. By making this transition, an impressive reduction of approximately 191,332 metric tons of CO_2 emissions can be achieved annually if this hydrogen is to be used as a fuel. This substantial decrease in greenhouse gas emissions contributes to the global effort to combat climate change and demonstrates the potential of hydrogen as a viable and eco-friendly fuel in the energy sector. However, in this study, hydrogen will be used as a feedstock for DME synthesis.

The evaluation of the microgrid system, as illustrated by the HYSYS and GAMS simulations, offers an insightful exploration into the domains of energy consumption, cost-effectiveness, environmental sustainability, and system optimization.

5.1. Energy Consumption Insights

The annual energy consumption of the microgrid system was quantified at 2.06×10^{12} kJ/yr. This emphasizes the critical need for energy efficiency measures. Specifically, the breakdown of electricity consumption at 4.23×10^7 kWh/year, alongside hot and cold utility consumption totaled at 1.17×10^{12} kJ/yr and 1.85×10^{12} kJ/yr, respectively, pinpoints the areas where energy demand is most pronounced. These results suggest that targeted initiatives to enhance the efficiency of electricity usage and thermal processes could significantly impact the system's overall energy footprint.

5.2. Economic Feasibility and Viability

The economic parameters offer a comprehensive view of the system's financial landscape. With a CapEx of USD 19,060,400, Operating Expenditure (OpEx) of USD 73,199,650 per year, and revenue of USD 105,989,621 per year, resulting in a profit of USD 13,729,571 per year, the data present a viable economic model for the microgrid's operation. These results not only affirm the financial feasibility of the microgrid system but also highlight the substantial role of operational management in sustaining profitability.

5.3. Carbon Efficiency and Environmental Performance

A standout aspect of the system's evaluation is its carbon efficiency, calculated at 86%. This efficiency demonstrates the system's adeptness at utilizing carbon resources, thereby minimizing greenhouse gas emissions. When considering the conversion rates—44.77% for the methanol synthesis reaction and 89.81% for the methanol dehydration reaction—the high carbon efficiency emphasizes the system's contribution to environmental sustainability. It highlights the potential of the microgrid system to align with global decarbonization goals.

5.4. Optimization of Heat Integration and Utility Costs

The application of HYSYS and GAMS for heat integration and utility cost optimization is particularly significant. The initial total utility costs, standing at USD 8,979,510/yr, were significantly reduced to USD 1,499,828/yr post-optimization, showing an 83% decrease. This dramatic reduction achieved by identifying the optimum combination of heating and cooling utilities—predominantly hot oil (93%) and low-pressure steam (7%) for heating, with cooling water (77%) and refrigerant (23%) for cooling—explains the potential for substantial cost savings through strategic system design and operation.

5.5. Future Implications and Research Directions

This research offers critical insights and directions for future sustainable, low-carbon energy systems in engineering. Future investigations might explore diverse electrolysis technologies, including solid oxide electrolysis, to enhance hydrogen production efficiency and evaluate their economic and environmental impacts. Additionally, research could focus on integrating emerging renewable energy sources, such as tidal or geothermal energy, into the microgrid system to further enhance its sustainability and efficiency. Addressing the challenge of intermittent renewable energy supply, especially pertaining to hydrogen production, is pivotal. Research could explore energy storage technologies, such as hydrogen storage, advanced battery systems, and kinetic storage, to stabilize the supply. Finally, developing advanced control and optimization algorithms for the microgrid system could improve its overall performance and adaptability to variable energy demands and weather conditions, paving the way for more resilient and robust energy infrastructures.

6. Conclusions

In this study, we examined and contrasted potential PtX alternatives, incorporating a techno-economic optimization that revealed the efficacy of each distinct hydrogen end-use option. The proposed renewable energy-based microgrid system demonstrates significant potential in terms of both economic feasibility and environmental benefits. By integrating PV plants, wind turbines, battery storage, and hydrogen electrolysis, the system offers a sustainable approach for simultaneous hydrogen production and DME synthesis. The in-depth analysis, encompassing economic evaluations, indicated an estimated annual profit of USD 13.70 million and identified alkaline water electrolysis as the most cost-effective option for hydrogen production.

Heat integration using a cascade table and GAMS optimizer led to an 83% reduction in annual utility costs, from USD 8,979,510 to USD 1,499,828. This over 50% reduction in energy consumption, compared to conventional reforming units, signifies a substantial advancement in energy efficiency, emphasizing its energy efficiency. The overall CO_2 emissions were assessed, and our integration approach led to a remarkable 99.24% reduction in emissions, demonstrating the system's potential in combating climate change.

Supplementary Materials: The following supporting information can be downloaded at: https://www.mdpi.com/article/10.3390/fuels5020011/s1, S1—Kinetic calculation. S2—Mass balance. S3—HEN Diagram Construction. S4—Cost optimization. Figure S1: Methanol synthesis phase mass balance. Figure S2: Methanol synthesis Excel spreadsheet. Figure S3: DME synthesis phase mass balance. Figure S4: DME synthesis Excel spreadsheet. Figure S5: HEN diagram building. Figure S6: Hot streams deficit energy. Figure S7: Cold streams deficit energy. Figure S8: Variables definition. Figure S9: Energy balance equations. Figure S10: Selected solver. Figure S11: Cost results and recommended utilities amount. Figure S12: Interval balance. Table S1: Degree of freedom analysis over methanol synthesis phase of the project. Table S2: Degree of freedom analysis over DME synthesis phase of the project.

Nomenclature

Abbreviation	Definition
AC	Alternating Current
BFD	Block Flow Diagram
CHP	Combined Heat And Power
CO_2	Carbon Dioxide
COE	Cost Of Energy
COE	Lowest Cost Of Energy
CP	Heat Capacity Mass Flow Rate
CP	Heat Capacity Mass Flow Rate
CRF	Capital Recovery Factor
CW	Cooling Water
CapEx	Total Capital Expenditure
DC	Direct Current
DME	Dimethyl Ether
DOD	Depth Of Discharge
GAMS	General Algebraic Modeling System
GHG	Greenhouse Gas
H_2	Hydrogen
HEN	Heat Exchanger Network
HMGs	Hybrid Microgrid Systems
HO	Hot Oil
HRES	Hybrid Renewable Energy Systems
IRENA	International Renewable Energy Agency
LCOE	Levelized Cost of Electricity
LCOH	Levelized Cost of Hydrogen
LP	Low Pressure
LPSP	Loss Of Power Supply Probability
N2	Nitrogen
NOCT	Nominal Operating Cell Temperature
NPV	Net Present Value
NS	Number Of Streams
NU	Total Number Of External Hot and Cold Utilities
O&M	Operation and Maintenance
OpEx	Total Operating Expenditure
PEM	Proton-Exchange Membrane
PEMFC	Polymer Electrolyte Membrane Fuel Cells
PRSV	Peng–Robinson Stryjek–Vera
P	Pressure in bar
PV	Photovoltaic
PtG	Power-to-Gas
PtL	Power-to-Liquids
PtX	Power-to-X
RE	Renewable Energy
RF	Renewable Fraction
RG	Refrigerant

RWGS	Reverse Water–Gas Shift
SOC	State of Charge
SOFC	Solid Oxide Fuel Cells
SOH	State of Hydrogen
SRK	Soave–Redlich–Kwong
SSO	Social Spider Optimizer
S_i	Selectivity Rate of Component i
T	Temperature in Kelvin
WT	Wind Turbines
X_i	Conversion Rate of Component i
Y_i	Yield Rate of Component i
kW	Kilowatts
kWh	Kilowatt-Hours

References

1. Azizi, Z.; Rezaeimanesh, M.; Tohidian, T.; Rahimpour, M.R. Dimethyl Ether: A Review of Technologies and Production Challenges. *Chem. Eng. Process. Process Intensif.* **2014**, *82*, 150–172. [CrossRef]
2. Arcoumanis, C.; Bae, C.; Crookes, R.; Kinoshita, E. The Potential of Di-Methyl Ether (DME) as an Alternative Fuel for Compression-Ignition Engines: A Review. *Fuel* **2008**, *87*, 1014–1030. [CrossRef]
3. Putrasari, Y.; Lim, O. Dimethyl Ether as the Next Generation Fuel to Control Nitrogen Oxides and Particulate Matter Emissions from Internal Combustion Engines: A Review. *ACS Omega* **2022**, *7*, 32–37. [CrossRef] [PubMed]
4. Peinado, C.; Liuzzi, D.; Sluijter, S.N.; Skorikova, G.; Boon, J.; Guffanti, S.; Groppi, G.; Rojas, S. Review and Perspective: Next Generation DME Synthesis Technologies for the Energy Transition. *Chem. Eng. J.* **2024**, *479*, 147494. [CrossRef]
5. Stepanenko, D.; Kneba, Z. DME as Alternative Fuel for Compression Ignition Engines—A Review. *Combust. Engines* **2019**, *58*, 172–179. [CrossRef]
6. Matzen, M.; Demirel, Y. Methanol and Dimethyl Ether from Renewable Hydrogen and Carbon Dioxide: Alternative Fuels Production and Life-Cycle Assessment. *J. Clean. Prod.* **2016**, *139*, 1068–1077. [CrossRef]
7. Leonzio, G. State of Art and Perspectives about the Production of Methanol, Dimethyl Ether and Syngas by Carbon Dioxide Hydrogenation. *J. CO2 Util.* **2018**, *27*, 326–354. [CrossRef]
8. Khalili, S.; Rantanen, E.; Bogdanov, D.; Breyer, C. Global Transportation Demand Development with Impacts on the Energy Demand and Greenhouse Gas Emissions in a Climate-Constrained World. *Energies.* **2019**, *12*, 3870. [CrossRef]
9. Galimova, T.; Ram, M.; Bogdanov, D.; Fasihi, M.; Gulagi, A.; Khalili, S.; Breyer, C. Global Trading of Renewable Electricity-Based Fuels and Chemicals to Enhance the Energy Transition across All Sectors towards Sustainability. *Renew. Sustain. Energy Rev.* **2023**, *183*, 113420. [CrossRef]
10. Breyer, C.; Lopez, G.; Bogdanov, D.; Laaksonen, P. The Role of Electricity-Based Hydrogen in the Emerging Power-to-X Economy. *Int. J. Hydrogen Energy* **2023**, *49*, 351–359. [CrossRef]
11. Bao, B.; El-Halwagi, M.M.; Elbashir, N.O. Simulation, Integration, and Economic Analysis of Gas-to-Liquid Processes. *Fuel Process. Technol.* **2010**, *91*, 703–713. [CrossRef]
12. An, Y.; Lin, T.; Yu, F.; Yang, Y.; Zhong, L.; Wu, M.; Sun, Y. Advances in Direct Production of Value-Added Chemicals via Syngas Conversion. *Sci. China Chem.* **2017**, *60*, 887–903. [CrossRef]
13. Marbán, G.; Valdés-Solís, T. Towards the Hydrogen Economy? *Int. J. Hydrogen Energy* **2007**, *32*, 1625–1637. [CrossRef]
14. IRENA Hydrogen from Renewable Power: Technology Outlook for the Energy Transition. 2018. Available online: https://www.irena.org/-/media/files/irena/agency/publication/2018/sep/irena_hydrogen_from_renewable_power_2018.pdf (accessed on 7 August 2023).
15. Bogdanov, D.; Ram, M.; Aghahosseini, A.; Gulagi, A.; Oyewo, A.S.; Child, M.; Caldera, U.; Sadovskaia, K.; Farfan, J.; De Souza Noel Simas Barbosa, L.; et al. Low-Cost Renewable Electricity as the Key Driver of the Global Energy Transition towards Sustainability. *Energy* **2021**, *227*, 120467. [CrossRef]
16. Quarton, C.J.; Tlili, O.; Welder, L.; Mansilla, C.; Blanco, H.; Heinrichs, H.; Leaver, J.; Samsatli, N.J.; Lucchese, P.; Robinius, M.; et al. The Curious Case of the Conflicting Roles of Hydrogen in Global Energy Scenarios. *Sustain. Energy Fuels* **2020**, *4*, 80–95. [CrossRef]
17. Bogdanov, D.; Gulagi, A.; Fasihi, M.; Breyer, C. Full Energy Sector Transition towards 100% Renewable Energy Supply: Integrating Power, Heat, Transport and Industry Sectors Including Desalination. *Appl. Energy* **2021**, *283*, 116273. [CrossRef]
18. Pursiheimo, E.; Holttinen, H.; Koljonen, T. Inter-Sectoral Effects of High Renewable Energy Share in Global Energy System. *Renew. Energy* **2019**, *136*, 1119–1129. [CrossRef]
19. Pfennig, M.; Böttger, D.; Häckner, B.; Geiger, D.; Zink, C.; Bisevic, A.; Jansen, L. Global GIS-Based Potential Analysis and Cost Assessment of Power-to-X Fuels in 2050. *Appl. Energy* **2023**, *347*, 121289. [CrossRef]
20. Chen, W.-H.; Hsu, C.-L.; Wang, X.-D. Thermodynamic Approach and Comparison of Two-Step and Single Step DME (Dimethyl Ether) Syntheses with Carbon Dioxide Utilization. *Energy* **2016**, *109*, 326–340. [CrossRef]

21. De Falco, M.; Capocelli, M.; Centi, G. Dimethyl Ether Production from CO$_2$ Rich Feedstocks in a One-Step Process: Thermodynamic Evaluation and Reactor Simulation. *Chem. Eng. J.* **2016**, *294*, 400–409. [CrossRef]

22. Luu, M.T.; Milani, D.; Sharma, M.; Zeaiter, J.; Abbas, A. Model-Based Analysis of CO$_2$ Revalorization for Di-Methyl Ether Synthesis Driven by Solar Catalytic Reforming. *Appl. Energy* **2016**, *177*, 863–878. [CrossRef]

23. Prasertsri, W.; Frauzem, R.; Suriyapraphadilok, U.; Gani, R. Sustainable DME Synthesis-Design with CO$_2$ Utilization. In *Computer Aided Chemical Engineering*; Elsevier: Amsterdam, The Netherlands, 2016; Volume 38, pp. 1081–1086.

24. Hankin, A.; Shah, N. Process Exploration and Assessment for the Production of Methanol and Dimethyl Ether from Carbon Dioxide and Water. *Sustain. Energy Fuels* **2017**, *1*, 1541–1556. [CrossRef]

25. Mevawala, C.; Jiang, Y.; Bhattacharyya, D. Techno-Economic Optimization of Shale Gas to Dimethyl Ether Production Processes via Direct and Indirect Synthesis Routes. *Appl. Energy* **2019**, *238*, 119–134. [CrossRef]

26. Michailos, S.; McCord, S.; Sick, V.; Stokes, G.; Styring, P. Dimethyl Ether Synthesis via Captured CO$_2$ Hydrogenation within the Power to Liquids Concept: A Techno-Economic Assessment. *Energy Convers. Manag.* **2019**, *184*, 262–276. [CrossRef]

27. Kartohardjono, S.; Adji, B.S.; Muharam, Y. CO$_2$ Utilization Process Simulation for Enhancing Production of Dimethyl Ether (DME). *Int. J. Chem. Eng.* **2020**, *2020*, 9716417. [CrossRef]

28. Rafiee, A. Staging of Di-Methyl-Ether (DME) Synthesis Reactor from Synthesis Gas (Syngas): Direct versus Indirect Route. *Chem. Eng. Res. Des.* **2020**, *163*, 157–168. [CrossRef]

29. Bernardi, A.; Chen, Y.; Chadwick, D.; Chachuat, B. Direct DME Synthesis from Syngas: A Technoeconomic Model-Based Investigation. In *Computer Aided Chemical Engineering*; Elsevier: Amsterdam, The Netherlands, 2020; Volume 48, pp. 655–660.

30. De França Lopes, G.; Bonfim-Rocha, L.; de Matos Jorge, L.M.; Paraíso, P.R. Dimethyl Ether Production from Sugarcane Vinasse: Modeling and Simulation for a Techno-Economic Assessment. *Bioenergy Res.* **2020**, *13*, 397–410. [CrossRef]

31. Schemme, S.; Breuer, J.L.; Köller, M.; Meschede, S.; Walman, F.; Samsun, R.C.; Peters, R.; Stolten, D. H2-Based Synthetic Fuels: A Techno-Economic Comparison of Alcohol, Ether and Hydrocarbon Production. *Int. J. Hydrogen Energy* **2020**, *45*, 5395–5414. [CrossRef]

32. Yasari, E.; Panahi, M.; Rafiee, A. Multi-objective Optimization and Techno-economic Analysis of CO$_2$ Utilization through Direct Synthesis of Di-methyl Ether Plant. *Int. J. Energy Res.* **2021**, *45*, 18103–18120. [CrossRef]

33. Wu, T.-W.; Chien, I.-L. A Novel Energy-Efficient Process of Converting CO$_2$ to Dimethyl Ether with Techno-Economic and Environmental Evaluation. *Chem. Eng. Res. Des.* **2022**, *177*, 1–12. [CrossRef]

34. Dieterich, V.; Neumann, K.; Niederdränk, A.; Spliethoff, H.; Sebastian, F. Techno-Economic Assessment of Renewable Dimethyl Ether Production Pathways from Hydrogen and Carbon Dioxide in the Context of Power-to-X. 2023; *preprint*. [CrossRef]

35. Veilleux, G.; Potisat, T.; Pezim, D.; Ribback, C.; Ling, J.; Krysztofiński, A.; Ahmed, A.; Papenheim, J.; Pineda, A.M.; Sembian, S.; et al. Techno-Economic Analysis of Microgrid Projects for Rural Electrification: A Systematic Approach to the Redesign of Koh Jik off-Grid Case Study. *Energy Sustain. Dev.* **2020**, *54*, 1–13. [CrossRef]

36. Klemm, C.; Vennemann, P. Modeling and Optimization of Multi-Energy Systems in Mixed-Use Districts: A Review of Existing Methods and Approaches. *Renew. Sustain. Energy Rev.* **2021**, *135*, 110206. [CrossRef]

37. Alzahrani, A.M.; Zohdy, M.; Yan, B. An Overview of Optimization Approaches for Operation of Hybrid Distributed Energy Systems with Photovoltaic and Diesel Turbine Generator. *Electr. Power Syst. Res.* **2021**, *191*, 106877. [CrossRef]

38. Bukar, A.L.; Tan, C.W. A Review on Stand-Alone Photovoltaic-Wind Energy System with Fuel Cell: System Optimization and Energy Management Strategy. *J. Clean. Prod.* **2019**, *221*, 73–88. [CrossRef]

39. Roy, A.; Auger, F.; Olivier, J.-C.; Schaeffer, E.; Auvity, B. Design, Sizing, and Energy Management of Microgrids in Harbor Areas: A Review. *Energies* **2020**, *20*, 5314. [CrossRef]

40. Babatunde, O.M.; Munda, J.L.; Hamam, Y. A Comprehensive State-of-the-Art Survey on Hybrid Renewable Energy System Operations and Planning. *IEEE Access* **2020**, *8*, 75313–75346. [CrossRef]

41. Singh, R.; Bansal, R.C. Review of HRESs Based on Storage Options, System Architecture and Optimisation Criteria and Methodologies. *IET Renew. Power Gener.* **2018**, *12*, 747–760. [CrossRef]

42. Kharrich, M.; Kamel, S.; Alghamdi, A.S.; Eid, A.; Mosaad, M.I.; Akherraz, M.; Abdel-Akher, M. Optimal Design of an Isolated Hybrid Microgrid for Enhanced Deployment of Renewable Energy Sources in Saudi Arabia. *Sustainability* **2021**, *13*, 4708. [CrossRef]

43. Fathy, A.; Kaaniche, K.; Alanazi, T.M. Recent Approach Based Social Spider Optimizer for Optimal Sizing of Hybrid PV/Wind/Battery/Diesel Integrated Microgrid in Aljouf Region. *IEEE Access* **2020**, *8*, 57630–57645. [CrossRef]

44. Alturki, A.A. Optimal Design for a Hybrid Microgrid-Hydrogen Storage Facility in Saudi Arabia. *Energy Sustain. Soc.* **2022**, *12*, 24. [CrossRef] [PubMed]

45. Zhang, Z.; Buttler, A.; Wienclaw, P.; Schmalzing, C.-O.; Siebert, J.; Flohr, A. Simulation Based Techno-Economic Evaluation of Self-Sufficient Microgrid Systems with Renewable Energy and Power-to-X. In *International Renewable Energy Storage Conference (IRES 2022)*; Atlantis Press: Amsterdam, The Netherlands, 2023; pp. 551–562.

46. De Falco, M.; Capocelli, M.; Basile, A. Selective Membrane Application for the Industrial One-Step DME Production Process Fed by CO$_2$ Rich Streams: Modeling and Simulation. *Int. J. Hydrogen Energy* **2017**, *42*, 6771–6786. [CrossRef]

47. Lee, B.; Lee, H.; Lim, D.; Brigljević, B.; Cho, W.; Cho, H.-S.; Kim, C.-H.; Lim, H. Renewable Methanol Synthesis from Renewable H$_2$ and Captured CO$_2$: How Can Power-to-Liquid Technology Be Economically Feasible? *Appl. Energy* **2020**, *279*, 115827. [CrossRef]

48. Semelsberger, T.A.; Ott, K.C.; Borup, R.L.; Greene, H.L. Role of Acidity on the Hydrolysis of Dimethyl Ether (DME) to Methanol. *Appl. Catal. B Environ.* **2005**, *61*, 281–287. [CrossRef]

49. Oar-Arteta, L.; Remiro, A.; Vicente, J.; Aguayo, A.T.; Bilbao, J.; Gayubo, A.G. Stability of $CuZnOAl_2O_3$/HZSM-5 and $CuFe_2O_4$/HZSM-5 Catalysts in Dimethyl Ether Steam Reforming Operating in Reaction–Regeneration Cycles. *Fuel Process. Technol.* **2014**, *126*, 145–154. [CrossRef]

50. Pontzen, F.; Liebner, W.; Gronemann, V.; Rothaemel, M.; Ahlers, B. CO_2-Based Methanol and DME–Efficient Technologies for Industrial Scale Production. *Catal. Today* **2011**, *171*, 242–250. [CrossRef]

51. Khunathorncharoenwong, N.; Charoensuppanimit, P.; Assabumrungrat, S.; Kim-Lohsoontorn, P. Techno-Economic Analysis of Alternative Processes for Alcohol-Assisted Methanol Synthesis from Carbon Dioxide and Hydrogen. *Int. J. Hydrogen Energy* **2021**, *46*, 24591–24606. [CrossRef]

52. Abdelaziz, O.Y.; Hosny, W.M.; Gadalla, M.A.; Ashour, F.H.; Ashour, I.A.; Hulteberg, C.P. Novel Process Technologies for Conversion of Carbon Dioxide from Industrial Flue Gas Streams into Methanol. *J. CO2 Util.* **2017**, *21*, 52–63. [CrossRef]

53. Bayomie, O.S.; Bouallou, C. Energy and Conversion Investigations of Different Process Configurations for Hydrogenation of CO_2 into Methanol from Industrial Flue Gases. *Chem. Eng. Trans.* **2018**, *70*, 1345–1350.

54. Van-Dal, É.S.; Bouallou, C. Design and Simulation of a Methanol Production Plant from CO_2 Hydrogenation. *J. Clean. Prod.* **2013**, *57*, 38–45. [CrossRef]

55. Turton, R.; Bailie, R.C.; Whiting, W.B.; Shaeiwitz, J.A. *Analysis, Synthesis and Design of Chemical Processes*; Pearson Education: Hoboken, NJ, USA, 2008.

56. Mignard, D.; Sahibzada, M.; Duthie, J.M.; Whittington, H.W. Methanol Synthesis from Flue-Gas CO_2 and Renewable Electricity: A Feasibility Study. *Int. J. Hydrogen Energy* **2003**, *28*, 455–464. [CrossRef]

57. Bejan, A. *Advanced Engineering Thermodynamics*; John Wiley & Sons: Hoboken, NJ, USA, 2016.

58. Shaikh, J.A. Techno-Economic Sizing and Optimization of Microgrid; A Case Study of A Higher Education Institution. *Int. J. Electr. Eng. Emerg. Technol.* **2021**, *4*, 37–40.

59. Lambert, T.; Gilman, P.; Lilienthal, P. Micropower System Modeling with HOMER. *Integr. Altern. Sources Energy* **2006**, *1*, 379–385.

60. Yang, H.; Zhou, W.; Lu, L.; Fang, Z. Optimal Sizing Method for Stand-Alone Hybrid Solar–Wind System with LPSP Technology by Using Genetic Algorithm. *Sol. Energy* **2008**, *82*, 354–367. [CrossRef]

61. Maleki, A.; Askarzadeh, A. Optimal Sizing of a PV/Wind/Diesel System with Battery Storage for Electrification to an off-Grid Remote Region: A Case Study of Rafsanjan, Iran. *Sustain. Energy Technol. Assess.* **2014**, *7*, 147–153. [CrossRef]

62. Boretti, A. *Hydrogen Key Technology to Cover the Energy Storage Needs of NEOM City*; Elsevier: Amsterdam, The Netherlands, 2022.

63. Salameh, T.; Sayed, E.T.; Abdelkareem, M.A.; Olabi, A.G.; Rezk, H. Optimal Selection and Management of Hybrid Renewable Energy System: Neom City as a Case Study. *Energy Convers. Manag.* **2021**, *244*, 114434. [CrossRef]

64. Hasan, S.; Shabaneh, R. *The Economics and Resource Potential of Hydrogen Production in Saudi Arabia*; KAPSARC: Riyadh, Saudi Arabia, 2021.

65. Heydari, A.; Askarzadeh, A. Optimization of a Biomass-Based Photovoltaic Power Plant for an off-Grid Application Subject to Loss of Power Supply Probability Concept. *Appl. Energy* **2016**, *165*, 601–611. [CrossRef]

66. Al-Sharafi, A.; Sahin, A.Z.; Ayar, T.; Yilbas, B.S. Techno-Economic Analysis and Optimization of Solar and Wind Energy Systems for Power Generation and Hydrogen Production in Saudi Arabia. *Renew. Sustain. Energy Rev.* **2017**, *69*, 33–49. [CrossRef]

67. Kalinci, Y.; Hepbasli, A.; Dincer, I. Techno-Economic Analysis of a Stand-Alone Hybrid Renewable Energy System with Hydrogen Production and Storage Options. *Int. J. Hydrogen Energy* **2015**, *40*, 7652–7664. [CrossRef]

68. Merei, G.; Berger, C.; Sauer, D.U. Optimization of an Off-Grid Hybrid PV–Wind–Diesel System with Different Battery Technologies Using Genetic Algorithm. *Sol. Energy* **2013**, *97*, 460–473. [CrossRef]

69. Fu, R.; Feldman, D.; Margolis, R.; Woodhouse, M.; Ardani, K. *US Solar Photovoltaic System Cost Benchmark: Q1 2017*; EERE Publication and Product Library: Washington, DC, USA, 2017.

70. Ralon, P.; Taylor, M.; Ilas, A.; Diaz-Bone, H.; Kairies, K. *Electricity Storage and Renewables: Costs and Markets to 2030*; International Renewable Energy Agency: Abu Dhabi, United Arab Emirates, 2017.

71. Schmidt, O.; Gambhir, A.; Staffell, I.; Hawkes, A.; Nelson, J.; Few, S. Future Cost and Performance of Water Electrolysis: An Expert Elicitation Study. *Int. J. Hydrogen Energy* **2017**, *42*, 30470–30492. [CrossRef]

72. Department of Energy U.S. *DOE Technical Targets for Hydrogen Production from Electrolysis*; Department of Energy U.S.: Washington, DC, USA, 2018.

73. Nykvist, B.; Nilsson, M. Rapidly Falling Costs of Battery Packs for Electric Vehicles. *Nat. Clim. Chang.* **2015**, *5*, 329–332. [CrossRef]

74. Bekele, Y.; Biru, G.; Tjernberg, L.B. Sustainable Off-Grid Systems with Integration of Renewable Generation and Hydrogen-Fuel Cell. In Proceedings of the 2022 IEEE PES Innovative Smart Grid Technologies Conference Europe (ISGT-Europe), Novi Sad, Serbia, 10–12 October 2022; pp. 1–5. [CrossRef]

75. Guangqian, D.; Bekhrad, K.; Azarikhah, P.; Maleki, A. A Hybrid Algorithm Based Optimization on Modeling of Grid Independent Biodiesel-Based Hybrid Solar/Wind Systems. *Renew. Energy* **2018**, *122*, 551–560. [CrossRef]

76. Ramli, M.A.M.; Bouchekara, H.R.E.H.; Alghamdi, A.S. Optimal Sizing of PV/Wind/Diesel Hybrid Microgrid System Using Multi-Objective Self-Adaptive Differential Evolution Algorithm. *Renew. Energy* **2018**, *121*, 400–411. [CrossRef]

77. Ding, Y.; Cano, Z.P.; Yu, A.; Lu, J.; Chen, Z. Automotive Li-Ion Batteries: Current Status and Future Perspectives. *Electrochem. Energy Rev.* **2019**, *2*, 1–28. [CrossRef]

78. James, B.D.; Houchins, C.; Huya-Kouadio, J.M.; DeSantis, D.A. *Hydrogen Storage System Cost Analysis*; Strategic Analysis Inc.: Arlington, VA, USA, 2016.

79. IRENA. *Low-Cost Finance for the Energy Transition*; International Renewable Energy Agency: Abu Dhabi, United Arab Emirates, 2023.

80. Towler, G.; Sinnott, R. *Chemical Engineering Design: Principles, Practice and Economics of Plant and Process Design*; Butterworth-Heinemann: Oxford, UK, 2021.

81. Seider, W.D.; Lewin, D.R.; Seader, J.D.; Widagdo, S.; Gani, R.; Ng, K.M. *Product and Process Design Principles: Synthesis, Analysis, and Evaluation*; John Wiley & Sons: Hoboken, NJ, USA, 2017.

82. Al-Qahtani, A.; Parkinson, B.; Hellgardt, K.; Shah, N.; Guillen-Gosalbez, G. Uncovering the True Cost of Hydrogen Production Routes Using Life Cycle Monetisation. *Appl. Energy* **2021**, *281*, 115958. [CrossRef]

83. Keith, D.W.; Holmes, G.; Angelo, D.S.; Heidel, K.; St. Angelo, D.; Heidel, K. A Process for Capturing CO_2 from the Atmosphere. *Joule* **2018**, *2*, 1573–1594. [CrossRef]

84. Kumar, V.; Saini, S.; Sharma, M.; Nigam, K.D.P. Pressure Drop and Heat Transfer Study in Tube-in-Tube Helical Heat Exchanger. *Chem. Eng. Sci.* **2006**, *61*, 4403–4416. [CrossRef]

85. Yusuf, N.; Almomani, F. Highly Effective Hydrogenation of CO_2 to Methanol over $Cu/ZnO/Al_2O_3$ Catalyst: A Process Economy & Environmental Aspects. *Fuel* **2023**, *332*, 126027.

86. Mignard, D.; Pritchard, C. Processes for the Synthesis of Liquid Fuels from CO_2 and Marine Energy. *Chem. Eng. Res. Des.* **2006**, *84*, 828–836. [CrossRef]

87. Sahibzada, M.; Metcalfe, I.S.; Chadwick, D. Methanol Synthesis from $CO/CO_2/H2$over $Cu/ZnO/Al_2O_3$at Differential and Finite Conversions. *J. Catal.* **1998**, *174*, 111–118. [CrossRef]

88. Atsonios, K.; Panopoulos, K.D.; Kakaras, E. Investigation of Technical and Economic Aspects for Methanol Production through CO_2 Hydrogenation. *Int. J. Hydrogen Energy* **2016**, *41*, 2202–2214. [CrossRef]

89. Wang, A.W.; Weigel, S.; Muraro, G. *Topical Report Molecular Sieves as Catalyst Methanol Dehydration*; Air Products and Chemicals Inc.: Allentown, PA, USA, 2002.

90. Liu, L.; Huang, W.; Gao, Z.; Yin, L. Synthesis of AlOOH Slurry Catalyst and Catalytic Activity for Methanol Dehydration to Dimethyl Ether. *J. Ind. Eng. Chem.* **2012**, *18*, 123–127. [CrossRef]

91. Bercic, G.; Levec, J. Intrinsic and Global Reaction Rate of Methanol Dehydration over. Gamma.-Alumina Pellets. *Ind. Eng. Chem. Res.* **1992**, *31*, 1035–1040. [CrossRef]

92. Jun, K.W.; Lee, H.S.; Roh, H.S.; Park, S.E. Catalytic Dehydration of Methanol to Dimethyl Ether (DME) over Solid-Acid Catalysts. *Bull. Korean Chem. Soc.* **2002**, *23*, 803–806.

93. Yaripour, F.; Mollavali, M.; Jam, S.M.; Atashi, H. Catalytic Dehydration of Methanol to Dimethyl Ether Catalyzed by Aluminum Phosphate Catalysts. *Energy Fuels* **2009**, *23*, 1896–1900. [CrossRef]

94. Farsi, M.; Eslamloueyan, R.; Jahanmiri, A. Modeling, Simulation and Control of Dimethyl Ether Synthesis in an Industrial Fixed-Bed Reactor. *Chem. Eng. Process. Process Intensif.* **2011**, *50*, 85–94. [CrossRef]

95. Kiss, A.A.; Ignat, R.M. Revamping Dimethyl Ether Separation to a Single-step Process. *Chem. Eng. Technol.* **2013**, *36*, 1261–1267. [CrossRef]

96. Leuenberger, H. New Trends in the Production of Pharmaceutical Granules: Batch versus Continuous Processing. *Eur. J. Pharm. Biopharm.* **2001**, *52*, 289–296. [CrossRef]

97. Goršek, A.; Glavič, P. Design of Batch versus Continuous Processes: Part I: Single-Purpose Equipment. *Chem. Eng. Res. Des.* **1997**, *75*, 709–717. [CrossRef]

98. Wetchakun, K.; Samerjai, T.; Tamaekong, N.; Liewhiran, C.; Siriwong, C.; Kruefu, V.; Wisitsoraat, A.; Tuantranont, A.; Phanichphant, S. Semiconducting Metal Oxides as Sensors for Environmentally Hazardous Gases. *Sensors Actuators B Chem.* **2011**, *160*, 580–591. [CrossRef]

99. Roode-Gutzmer, Q.I.; Kaiser, D.; Bertau, M. Renewable Methanol Synthesis. *ChemBioEng Rev.* **2019**, *6*, 209–236. [CrossRef]

100. Zhang, C.; Jun, K.-W.; Kwak, G.; Lee, Y.-J.; Park, H.-G. Efficient Utilization of Carbon Dioxide in a Gas-to-Methanol Process Composed of CO_2/Steam–Mixed Reforming and Methanol Synthesis. *J. CO2 Util.* **2016**, *16*, 1–7. [CrossRef]

101. Diaz, L.F.; Bertoldi, M.; Bidlingmaier, W.; Stentiford, E. *Compost Science and Technology*; Elsevier: Amsterdam, The Netherlands, 2007.

102. Baldea, M.; Daoutidis, P.; Kumar, A. Dynamics and Control of Integrated Networks with Purge Streams. *AIChE J.* **2006**, *52*, 1460–1472. [CrossRef]

103. Fogler, H.S. *Essentials of Chemical Reaction Engineering*; Pearson Education: Hoboken, NJ, USA, 2017; Volume 2017. [CrossRef]

104. Langmuir, I. The Constitution and Fundamental Properties of Solids and Liquids. II. Liquids. *J. Am. Chem. Soc.* **1917**, *39*, 1848–1906. [CrossRef]

105. Saeid, N.H.; Seetharamu, K.N. Finite Element Analysis for Co-current and Counter-current Parallel Flow Three-fluid Heat Exchanger. *Int. J. Numer. Methods Heat Fluid Flow* **2006**, *16*, 324–337. [CrossRef]

106. Perry, R. *Perry's Chemical Engineers' Handbook*, 9th ed.; Green, D.W., Southard, M.Z., Eds.; McGraw-Hill Education: New York, NY, USA, 2019.

107. Xu, M.; Lunsford, J.H.; Goodman, D.W.; Bhattacharyya, A. Synthesis of Dimethyl Ether (DME) from Methanol over Solid-Acid Catalysts. *Appl. Catal. A Gen.* **1997**, *149*, 289–301. [CrossRef]

108. Nguyen, T.; Abdin, Z.; Holm, T.; Mérida, W. Grid-Connected Hydrogen Production via Large-Scale Water Electrolysis. *Energy Convers. Manag.* **2019**, *200*, 112108. [CrossRef]

109. Pérez-Fortes, M.; Schöneberger, J.C.; Boulamanti, A.; Tzimas, E. Methanol Synthesis Using Captured CO_2 as Raw Material: Techno-Economic and Environmental Assessment. *Appl. Energy* **2016**, *161*, 718–732. [CrossRef]
110. Townsend, D.W.; Linnhoff, B. Designing Total Energy Systems by Systematic Methods. *Chem. Eng.* **1982**, *378*, 91–97.